Journal of Fluids and Structures 102 (2021) 103225

Contents lists available at ScienceDirect

Journal of Fluids and Structures

journal homepage: www.elsevier.com/locate/jfs

Steady and unsteady loading on a hydrofoil immersed in a turbulent boundary layer

Samuel M. Smith [a], Paul A. Brandner [a,*], Bryce W. Pearce [a], James A. Venning [a], Danielle J. Moreau [b], David B. Clarke [c]

[a] Australian Maritime College, University of Tasmania, Launceston, Tasmania 7250, Australia
[b] School of Mechanical and Manufacturing Engineering, University of New South Wales, Sydney, New South Wales 2052, Australia
[c] Defence Science and Technology Group, Fishermans Bend, Victoria 3207, Australia

ARTICLE INFO

Article history:
Received 23 February 2020
Received in revised form 22 September 2020
Accepted 6 January 2021
Available online 30 January 2021

Keywords:
Unsteady loading
Turbulent boundary layer
Hydrofoil

ABSTRACT

The steady and unsteady loads acting on a hydrofoil immersed in a turbulent boundary layer have been investigated. Measurements were performed in a cavitation tunnel in which the hydrofoil was mounted from the test section ceiling, via a 6-component force balance. Two NACA0012 hydrofoil models with trapezoidal planforms and aspect ratios of 2.4 and 1.2 were examined. The ceiling turbulent boundary layer was artificially thickened via an array of transverse jets located upstream of the test section. Thickening the ceiling boundary layer allowed for varying levels of hydrofoil immersion (nominally up to 100%) to be studied. In addition to the level of immersion, the effect of varying incidence and Reynolds number on the hydrodynamic loading normal to the chord was also investigated. Steady forces were found to be significantly affected by the relative scale of the boundary layer, particularly in the stall region. A broadband peak in the unsteady normal force spectra was observed at a constant reduced frequency of 0.2. The relative peak amplitude was found to be dependent on the boundary layer thickness to hydrofoil span ratio and Reynolds number. As the incidence is increased past stall, a low-frequency power increase was observed which was superimposed over the existing broadband excitation induced by the ceiling boundary layer.

1. Introduction

Control surfaces for marine vessels are typically located at the stern, where the boundary layer has had the full vessel length to develop and thicken. In addition, the boundary layer may be further thickened with the occurrence of flow separation due to the adverse pressure gradient present at the aft end of a vessel (Alin et al., 2010). As control surfaces are generally compact compared to overall length scales, they may be substantially immersed within the turbulent flow about the vessel stern. Hence, these control surfaces are subject to unsteady loading and become a source of vibration and radiated noise. To minimize these effects, insight into the flow physics and excitation spectra are required. This would enable a more rigorous analysis and design for control surface optimization including the structural response.

Much of the previous work into understanding and predicting the unsteady loading on lifting or control surfaces has been motivated by aeronautical applications involving the prediction of radiated noise and undesirable structural responses (e.g. buffeting). The problem of unsteady aerofoil loading has received considerable attention since the initial

* Corresponding author.
E-mail addresses: ssmith18@utas.edu.au (S.M. Smith), p.brandner@utas.edu.au (P.A. Brandner).

https://doi.org/10.1016/j.jfluidstructs.2021.103225
0889-9746/

work by Theodorsen (1935) who simplified the problem to an oscillating flat plate encountering an oncoming uniform flow. This work was developed further by von Kármán and Sears (1938) using basic concepts of circulation theory to establish a unified treatment of unsteady aerofoil theory. This work set the basis for Sears (1941) who treated the problem as a rigid aerofoil encountering vortical sinusoidal gusts. Using linearized inviscid theory, Sears (1941) derived the well-known expression for the lift function, known as the Sears function, which would eventually serve as the foundation to a significant body of future work in which key advancements have been made (Atassi, 1984).

In an attempt to validate the results from prediction models, early experiments were conducted by Lamson (1956) and Hakkinen and Richardson Jr (1957). Issues arose with obtaining conclusive results as the experimental data exhibited excessive scatter attributed to the turbulence scales present being too small to cause sufficient fluctuations in the unsteady loading. This remained an issue for many years, until Jackson et al. (1973) successfully measured the lift on a finite wing in grid turbulence. It was observed that the lift drops off faster than that predicted by Sears 2D strip theory at the high end of the spectrum which was attributed to the increasing importance of viscous and boundary layer displacement effects at higher frequencies (Li et al., 2018).

In order to calculate the rapidly changing turbulent flow due to large scale velocity gradients and foil interaction, Goldstein and Atassi (1976) and Atassi (1984) implemented Rapid Distortion Theory (RDT). This would take into account the effect of gust distortion, proving to be important in experiments conducted by McKeough and Graham (1980) as RDT predicts that the vertical velocity variance increases with turbulent flow progressing along a body. The results revealed that mean incidence only has significant effect on the loading spectra at low frequencies. Prediction models continued to develop with the introduction of vortex lift theory by Howe (2001, 2002) which took into account various forms of unsteady flow. The effect of aerofoil geometry such as thickness and camber, as well as incidence, became of key interest with significant advancements made by Reba and Kerschen (1996) and Glegg and Devenport (2009). Despite the extensive development of theoretical models there are relatively few complimentary experimental studies, such as those by Jackson et al. (1973) and McKeough and Graham (1980), to validate the analytical predictions. Mish and Devenport (2006a,b) note this as a motivation for their extensive wind tunnel experiments additional to numerical studies.

The experimental investigations by Mish and Devenport (2006a) involved a two dimensional NACA0015 aerofoil immersed in grid-generated turbulence with lift spectra derived from surface pressure measurements via an array of 96 microphones distributed along the chord and span. Experiments were conducted at a Reynolds number (Re) of 1.17×10^6 for incidences ranging from 0° to 20° where they observed a reduction in the surface pressure spectral level at low reduced frequencies, $f' = fc/U$, as the incidence was increased. The opposite effect was observed at higher f', with the cross over occurring at $f' = 5$ for all incidences. These results were in contrast to the earlier experimental observations made by McKeough and Graham (1980) and theoretical formulations by Atassi (1984) and Reba and Kerschen (1996). Mish and Devenport (2006b) attributed the low f' reduction in loading spectra to distortion of the oncoming flow by the mean velocity field. It was also noted that this effect was only significant when the relative scale of the inflow turbulence to aerofoil chord is sufficiently small ($< 13\%$).

The influence of free stream turbulence (FST) intensity on the performance characteristics on a lifting surface has been extensively investigated and shown to have significant quantitative and qualitative effects (Hoffmann, 1991; Huang and Lee, 1999; Devinant et al., 2002). Experiments conducted by Hancock and Bradshaw (1983) showed an increase in skin friction of a flat plate boundary layer when encountering increased FST. When exposed to an adverse pressure gradient, Hoffmann and Kassir (1988) observed a higher resistance to separation due to increased momentum transmission from the free stream to the boundary layer. This resistance to separation is seen on aerofoils encountering FST intensities varying from 0.25% and 16.00% (Hoffmann, 1991; Devinant et al., 2002; Wang et al., 2014). This momentum or turbulent kinetic energy (TKE) transfer encourages shear layer transition along with a reduction in the integral length scale to boundary layer thickness ratio, thus resulting in a resistance to separation. With aerofoil performance shown to be significantly affected, not just by intensity level, but by the integral length scales as well, the embedded turbulence of a boundary layer poses an extra degree of complexity due to the various length scales involved (Smits et al., 2011).

It has been shown by Swalwell et al. (2001) that the separation and re-attachment of an aerofoil boundary layer is significantly influenced by the Re and FST of the oncoming flow. Hence, the degree of intensity and Re of the flow can either cause or prevent the formation of a separation bubble (Li et al., 2011; Samson and Sarkar, 2016), and is also a known source of vortex shedding, and therefore unsteady loading (Mayda et al., 2002). Additionally, Devinant et al. (2002) showed that variations in the aerodynamic properties due to changes in Re of wind turbine blades, such as lift, drag, pitching moment and pressure distribution, were reduced when encountering high levels of FST intensity ($I > 12\%$). A turbulence intensity threshold identified by Huang and Lee (1999) shows that increases in turbulence intensity past 0.45% has minimal effect to the flow regime.

In a maritime context, insight into the flow phenomena and dynamic response involved with flow-induced vibrations of a hydrofoil due to unsteady loading is of significant interest. Ducoin et al. (2012a) experimentally characterized the laminar to turbulent transition induced vibrations on a hydrofoil. With further investigation, Ducoin et al. (2012b) also observed vortex shedding from the laminar separation bubble as well as dual frequency vortex shedding from the leading edge to cause vibration. One critical aspect noted in these investigations, and highlighted in the work by Zarruk et al. (2014), is the natural frequency of a hydrofoil. In the situation where a flow-induced vibration frequency coincides with the natural frequency, the resulting amplification in tip deflections (resonance) may result in undesirable through to critical conditions.

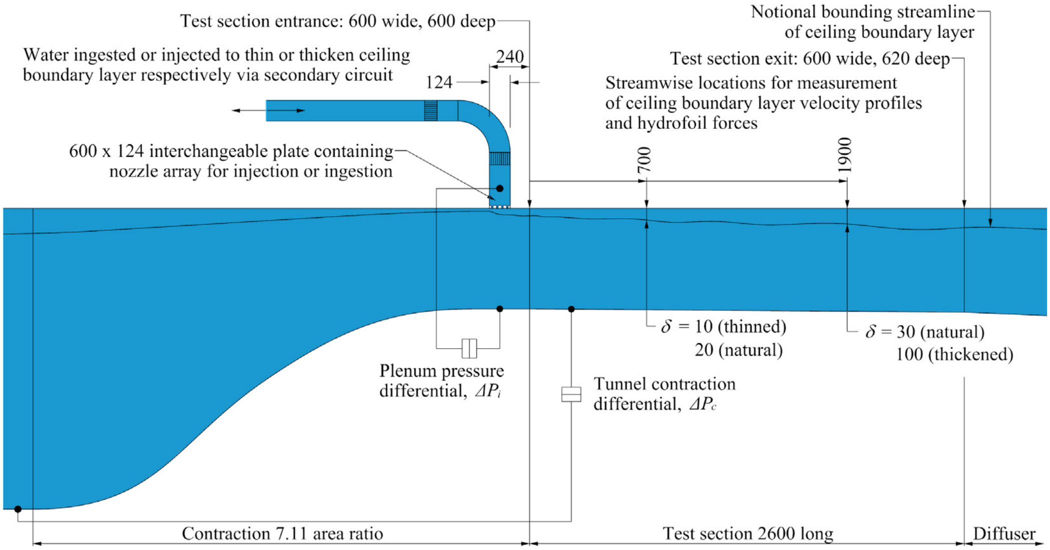

Fig. 1. Schematic of the control system for thickening of the test section ceiling boundary layer using an array of cross flows jets. The boundary layer thickness is controlled using the jet plenum static pressure relative to the freestream dynamic pressure. (All dimensions are in mm).

Recent experiments by Lysak (2011) and Lysak et al. (2016) have obtained loading spectra from hydrofoils of various thickness encountering grid turbulence that closely resemble theoretical predictions. Comparing the experimental results with their adaptation of vortex lift theory (Howe, 2001), Lysak et al. (2013) accurately predicted the high-frequency reduction in the loading spectra as thickness increases. Suggestions for future work by Lysak (2011) highlight the importance to further investigate the effect of incidence and camber on the loading spectra as well as overcoming background vibration contamination to analyse higher frequencies. The importance of these suggestions is highlighted in work by Khoo et al. (2015) who measured the unsteady loading on a NACA0012 hydrofoil where a significant increase in the loading spectra is observed, particularly at low frequencies, when transitioning to stall. In addition, the resolvable frequency range was limited due to the inherent dynamic response from the coupled force balance/hydrofoil system, similar to that experienced by Lysak et al. (2016). Despite this extensive theoretical, numerical and experimental activity on the unsteady loading on a lifting surface encountering grid turbulence, there is a paucity of published material on the related topic of encountering structured turbulence, such as a boundary layer.

The present study aims to provide additional insights into the physics determining the loading of a hydrofoil encountering the structured turbulence of an oncoming boundary layer. Forces, both steady and unsteady, are obtained for a range of Reynolds numbers (Re), incidence (α) and boundary layer thicknesses (δ). Immersion of the hydrofoil span in the boundary layer is adjusted from around $\frac{1}{8}$ to the full span. These results provide design guidance for the development of high-performance appendages encountering a boundary layer. Additionally, the data obtained will aid in determining the frequency response necessary from an improved force balance and model design for future unsteady force measurements.

2. Experimental overview

2.1. Experimental setup

Measurements were carried out in the Cavitation Research Laboratory (CRL) water tunnel at the Australian Maritime College. The tunnel test section is 0.6 m square by 2.6 m long in which the operating velocity and pressure ranges are 2 to 12 m/s and 4 to 400 kPa absolute, respectively. The tunnel volume is 365 m^3 with demineralized water (conductivity of order 1 μS/cm). The test section velocity is measured from one of two (high and low range) Siemens Sitransp differential pressure transducers models 7MF4433-1DA02-2AB1-Z and 7MF4433-1FA02-2AB1-Z (measuring the calibrated contraction differential pressure) with estimated precisions of 0.007 and 0.018 m/s, respectively. A detailed description of the facility is given in Brandner et al. (2007).

A schematic representation of the test set-up is given in Fig. 1 with definition of the coordinate system used and the main geometric parameters shown in Fig. 2. The models were mounted on either a static or dynamic 6-component force balance. The hydrofoils extended vertically into the flow through a 160 mm diameter penetration in the tunnel ceiling. The 160 mm diameter penetration was made fair (to 50 μm) using a disc mounted on the measurement side of the balance. The fairing disc has a nominal 0.5 mm radial clearance to avoid interference with the force measurement. Of the total load vector measured, steady and unsteady components of normal force, axial force and pitching moment are presented. Spanwise forces and roll/yaw moments are not considered as they may be contaminated by the ceiling

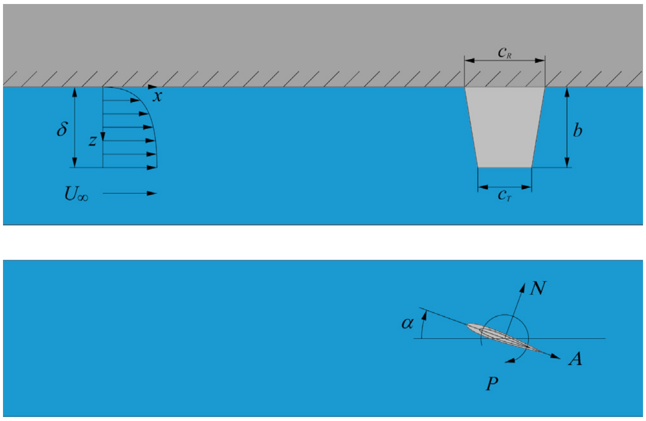

Fig. 2. Schematic of the experimental setup whereby a ceiling mounted hydrofoil encounters the turbulent boundary layer. The hydrofoil and boundary layer coordinate systems are shown with the hydrofoils origin located at the root along the centreline at mid-chord. The hydrofoil is immersed to varying degrees by artificially thickening the ceiling boundary layer.

Table 1
Natural frequencies, mass and added mass values of the model hydrofoils utilized in the experiment with added mass estimates calculated as per the method of Blevins (1979).

Hydrofoil Dynamic Properties	Hydrofoil span	
	120 mm	240 mm
First bending mode in air (Hz)	536	170
First bending mode in water (Hz)	273	86
Second bending mode in air (Hz)	–	783
Second bending mode in water (Hz)	–	399
Added mass for first and second bending modes, $2m_a$ (kg)	0.94	1.88
Mass of hydrofoil, m (kg)	0.33	0.60

pressure distribution acting on the disc with this setup. Measurements were made at streamwise locations of 0.7 and 1.9 m downstream from the test section entrance to maximize the range of hydrofoil immersion in the ceiling boundary layer. Data was sampled at 1024 Hz for durations sufficient to capture 1000 and 22,000 chord passages, $n = TU_\infty/c$, where T is the acquisition period, U_∞ is the freestream velocity and c is the mean chord, for steady and unsteady measurements, respectively. Test section free-stream velocity was varied to achieve chord-based Reynolds numbers, $Re = U_\infty c/\nu$, ranging from 0.4×10^6 to 1.2×10^6, where ν is the kinematic viscosity of the water.

2.2. Model hydrofoil details

Hydrofoil geometry has been selected based on the requirements discussed above for the modelling of unsteady conditions typical of those experienced by control surfaces. The chosen geometry was a NACA0012 profile with a symmetric (unswept) trapezoidal planform with a 80 mm tip and 120 mm root chord. Two models were constructed with spans (b) of 120 mm and 240 mm giving aspect ratios (b/c) of 1.2 and 2.4, respectively. This achieved a wide range of oncoming ceiling boundary layer thickness to hydrofoil span ratios, δ/b, from 0.08 up to 0.90 (with δ being the thickness where the streamwise velocity is equal to $0.99U_\infty$). The chord length was chosen to be compatible with mounting to the water tunnel test section and sufficient to obtain Re values of 1.2×10^6.

The response spectrum of both hydrofoils was determined from an impact test by Khoo et al. (2015) with results summarized in Table 1. First-mode natural frequencies were obtained in air at 536 Hz and 170 Hz, and in-water at 273 and 86 Hz for the 120 mm and 240 mm models, respectively. These frequencies are with the hydrofoils mounted to the static force balance (described in Section 2.3) as a slight increase in the natural frequencies was observed when mounted in a rigid configuration. The mode shapes of the hydrofoils were predicted based on unpublished results from experiments conducted by Clarke et al. (2014) as well FEA modal analyses. The results showed the first mode of both hydrofoils as well as the second mode of the 240 mm hydrofoil were all of the bending type. To predict the in-water natural frequencies added mass estimations were calculated using formulas from Blevins (1979) where the hydrofoil was treated as a cantilevered rectangular flat plate. Both models were machined from solid Aluminium 6061-T6 billets to 0.8 μm surface finish and 0.1 mm surface tolerance. The models were anodized to a thickness of approximately 5 μm.

A body-fixed coordinate system was used to define the loads acting on the hydrofoil which is presented in Fig. 2. The normal force, N, axial force, A, and pitching moment, P, acting on the hydrofoils are presented as dimensionless coefficients with $C_N = 2N/\rho U_\infty^2 cb$, $C_A = 2A/\rho U_\infty^2 cb$ and $C_P = 2P/\rho U_\infty^2 c^2 b$, respectively. The unsteady component of

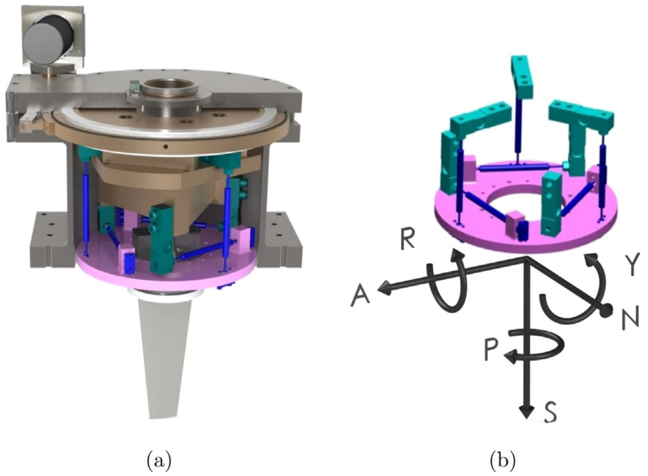

Fig. 3. Static force balance configuration showing (a) casing sectioned view, with a hydrofoil attached, to show internal assembly and (b) load cell and flexure layout on the measurement side console (in pink) with the coordinate system used as shown.

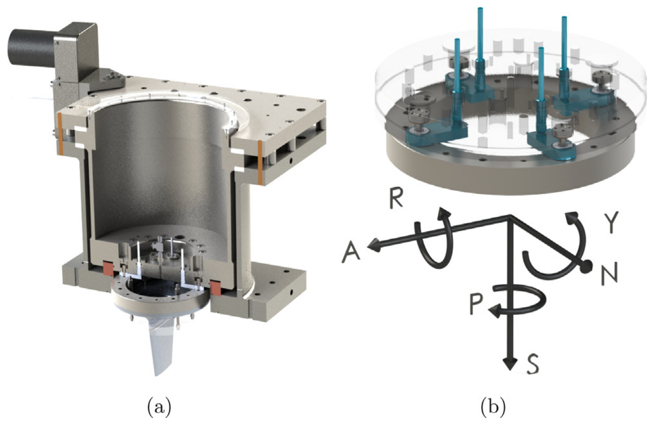

Fig. 4. (a) Dynamic force balance section view and (b) a view showing the orientation of the four Kislter 9602 piezoelectric loadcells. The loadcells (teal) are preloaded between a non-measurement (transparent) and measurement side console (grey), with the coordinate system used defined as shown.

the forces is represented with $'$ denoting the standard deviation of the time varying quantities. The centre of pressure, x_{cop}, is calculated as $x_{cop} = (c/2 - P/N)$ where $x_{cop}/c = 0.0$ and 1.0 denotes the leading and trailing edge, respectively, at midspan of the hydrofoil. To utilize the large dataset obtained using the static force balance to gain insight on the unsteady component, the time series required filtering to remove the static force balance response from the spectra. This was achieved by applying an infinite impulse response lowpass filter to the time series with a cut-off frequency of 100 Hz and a steepness value of 0.95. The standard deviation calculated from the filtered time series compared favourably with those obtained from the dynamic force balance with the filtered standard deviation values presented in Section 3.2.

2.3. Static and dynamic force balances

To obtain both steady as well as unsteady forces with a high resolvable frequency range, two force balances were utilized. Steady forces were measured using a '*static*' force balance incorporating six MTI 4856-500 beam load cells and flexures to connect the measurement and non-measurement consoles of the balance (Fig. 3). The static force balance is relatively electronically stable with sensor drift seen to be negligible over measurements spanning many hours making it suitable for steady force measurements. The natural frequency of the static force balance is measured to be between 139 and 148 Hz (Khoo et al., 2015). For unsteady force measurements, the dynamic force balance (Fig. 4) was utilized for its increased resolvable frequency range compared to the static force balance. A '*dynamic*' force balance features four 3-component Kistler 9602 piezoeletric force sensors with integrated charge amplifier electronics that are compressed between the measurement and non-measurement consoles. The high stiffness of the piezoelectric force sensors in combination with force balance architecture results in a maximum resolvable frequency of approximately 1000 Hz.

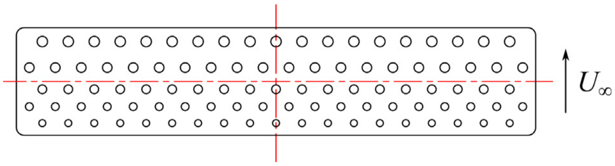

Fig. 5. Test plate used in the artificial thickening of the oncoming ceiling boundary layer. The plate features a nozzle configuration with triangular spacing and varying nozzle diameter as detailed in Table 2.

Table 2
Geometric properties of the artificial thickening plate which featured rows of holes where the diameter of the first row of holes was equal to 8 mm. The hole diameter increases by 1 mm in the following row in the downstream direction, with the last row hole diameter being 12 mm.

Property	Value
Number of holes	97
Hole diameter (mm)	8–12
Bellmouth radius (mm)	5
Open area (mm^2)	7769
Streamwise hole spacing (mm)	30-19
Transverse hole spacing (mm)	30
Plate thickness (mm)	15

The calibration of both the static and dynamic force balance is performed on a purpose-built calibration frame. An accurately machined mounting plate and calibration arm is attached to the measurement side disc of the force balances to which static forces are applied in six orientations, loading the force balance in the A, N, S, R, Y and P directions (Figs. 3 and 4). The static forces are generated using precision weights and gravity that are either directly slung off the calibration arm or via an air bearing depending on the loading orientation. Static calibration of the dynamic force balance is made possible by integrated charge amplifier electronics in the piezoelectric force sensors that result in sufficiently low drift that can be compensated for by employing a pilgrim step loading technique (Mack, 2006).

The static force balance was calibrated by a least squares fit between a basis vector loading cycle and the 6 outputs giving a 6×6 matrix. The dynamic force balance was calibrated by a least squares fit between a basis vector loading cycle and the 12 outputs to produce a 12×6 matrix. The calibration matrix was calculated by taking the right pseudo-inverse of the non-square voltage matrix using the Moore–Penrose method and multiplying it with the force matrix. The estimated precision of all components for the static and dynamic force balances are less than 0.1% and 0.5%, respectively.

Forces were measured at a set of mean chord-based Reynolds numbers, $Re = U_\infty c/\nu$, where ν is the kinematic viscosity and c denotes the mean chord, $c = (c_T + c_R)/2 = 0.1$ m, with the subscripts T and R representing the tip and root of the hydrofoil. Measurements were conducted at Re values ranging from 0.2×10^6 to 1.2×10^6 in increments of 0.2×10^6. For each Re value, force measurements were acquired over the range of α from $-1°$ to beyond stall. The upper limit varied between 25° and 20° for the 120 mm and 240 mm span hydrofoils, respectively. The incidence was adjusted using the balance automated indexing system incremented in 0.5° steps with an incremental precision less than 0.001°. The tunnel was pressurized up to 350 kPa to suppress cavitation occurrence for all test conditions.

2.4. Boundary layer manipulator

To obtain a test section ceiling boundary layer of the desired scale, it was artificially thickened via an array of cross flow jets located upstream of the test section. At the test locations, the boundary layer thickness, δ, at which the mean velocity, $U = 0.99U_\infty$, was adjusted from its natural state of 19.1 mm at $x = 0.7$ m, to a maximum of 107.4 mm at $x = 1.9$ m. The boundary layer thickness, δ, was controlled by adjustment of the flow rate through the jet array. A detailed description and performance characteristics of the CRL boundary layer manipulator is given in Belle et al. (2016). Based on the performance of the plate geometries previously tested for boundary layer thickening, a revised design (Fig. 5) was developed to optimize the velocity profile in the outer or wake region. It is this region which extends over the largest portion of the boundary layer thickness and it contains the larger turbulent structures. The plate features 5 rows of holes in a triangular configuration which increase in diameter in the downstream direction. A summary of key geometrical properties of the plate is given in Table 2.

The artificial boundary layer thickness was varied by adjusting the mass flux, or jet, to freestream velocity ratio which is controlled and set by the injection pressure coefficient, given by:

$$C_{pi} = \frac{p_i - p_\infty}{\frac{1}{2}\rho U_\infty^2} \quad (1)$$

where p_i is the injection pressure and p_∞ is the free stream static pressure (see Fig. 1 for the pressure measurement locations). C_{pi} was varied between 0.04 and 0.62 to obtain a wide range of boundary layer thickness to span ratios, δ/b.

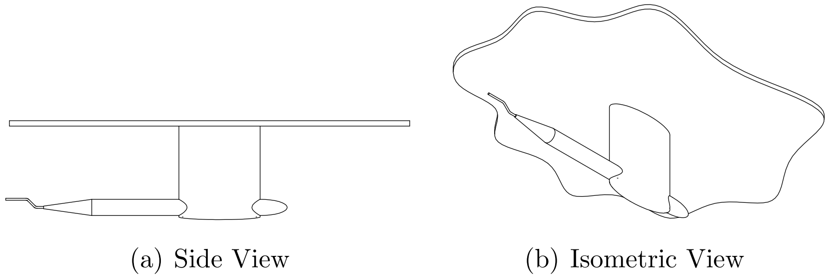

Fig. 6. Elliptical stem total head tube used for measurement of the natural and thickened boundary layer mean velocity profiles. The major and minor diameters of the elliptical stem are 30 and 10 mm. The tubes have a inner and outer diameter of 0.72 and 0.4 mm respectively. The total head tube on the elliptical stem probe is cranked in the vertical plane to enable the probe to be traversed to the ceiling for Preston tube measurements.

2.5. Boundary layer measurements

Boundary layer mean velocities were obtained using a 0.7 mm outside, by 0.4 mm inside, diameter total head tube traversed along the vertical centre plane of the test section. A wall reference static tapping of 1 mm diameter was located on the test section ceiling 75 mm off the centre plane. The total head tube was mounted within a support tube that tapered from 0.7 mm at the probe head to 6 mm. The support tube was mounted to a 30 mm by 10 mm elliptical stem section that penetrated through the test section ceiling (Fig. 6). The total head tube was traversed using an automated linear traverse with an estimated precision of 3 μm. Long-range macro-optics and back-lighting were used to establish the probe position on the ceiling. Pressures were measured using a Validyne Model DP15TL differential pressure transducer via an automated pressure multiplexer.

Boundary layer velocity profile measurements were comprised of 50 data points on a log distribution being sampled at 1024 Hz. Measurements were taken for durations sufficient to capture a minimum of 5000 boundary layer turnover times (TU_∞/δ), where T is the measurement duration, sufficient to obtain converged results (Belle et al., 2016). Preston tube measurements provided the wall shear stress, τ_w, using the calibration by Head and Ram, as presented in Goldstein (1996). Pitot probe corrections were applied to the measurements following the method outlined in Bailey et al. (2013) where shear layer and wall proximity effects were taken into account using equations by McKeon et al. (2003). These corrections were applied in the same manner as detailed by Belle et al. (2016). All boundary layer measurements were conducted at $Re = 1 \times 10^6$.

2.6. Electrical noise removal technique

The design of the dynamic force balance to possess a high natural frequency incorporated piezoelectric force sensors due to their high stiffness, which in turn have a low sensitivity. This results in a low signal to noise ratio and force measurements that are contaminated by electrical noise, particularly at the mains frequency of 50 Hz and its harmonics. To overcome this, a modified version of the noise removal technique developed by Alamshah et al. (2013) was used. This technique which was initially developed for the removal of wind-induced noise in shielded microphones utilizes cross-spectral analysis to obtain the incoherent output power (IOP) that distinguishes the contribution of one signal from another. The advantage of using the modified IOP method over a notch filter is that only the electrical noise contribution would be removed, rather than all signal components.

The modified IOP method was applied to the datasets by first determining the magnitude-squared coherence, γ^2, between the normal force and one of the voltage channels. This was achieved using the auto-spectra of the normal force and voltage channel, $G_{NN}(f)$ and $G_{VV}(f)$ respectively, along with the cross spectrum of the two signals, $G_{VN}(f)$, as shown in Eq. (2). The voltage channel used in the modified IOP method was one of the force components of a transducer mounted in the dynamic force balance that was found not to respond to any applied load. This channel was connected to the same system and electrically identical to the other force channels, exposing it to the same electrical contamination.

$$\gamma^2 = \frac{|G_{VN}(f)|^2}{G_{VV}(f)G_{NN}(f)} \tag{2}$$

Some coherency exists between the two signals at frequencies other than 50 Hz and its harmonics. To avoid removing components of the signal at these other frequencies, the IOP method was modified to consider only a 6 Hz bandwidth at 50 Hz and harmonics. This was achieved when calculating the IOP of the normal force auto-spectrum in Eq. (3), by setting the coherence value to zero for frequencies that lie outside of the bandwidth. The IOP normal force spectra are presented in Section 3.3.

$$IOP(f) = \left[1 - \gamma^2(f)\right] G_{NN}(f) \tag{3}$$

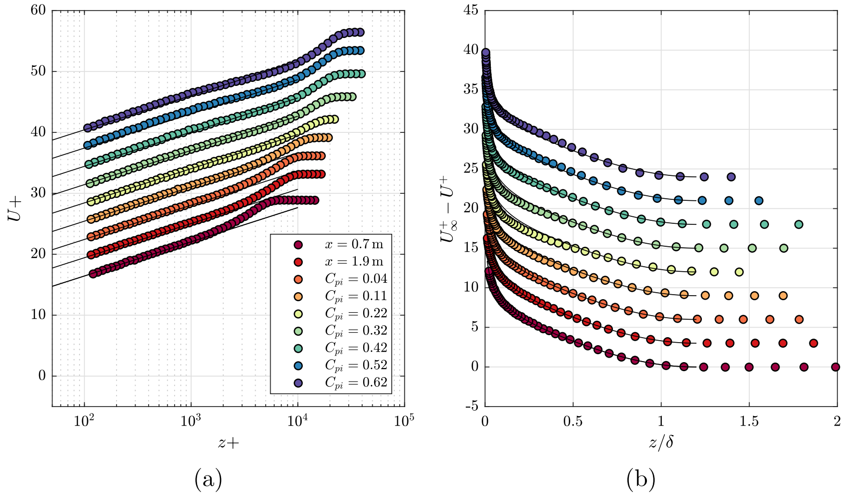

Fig. 7. Variation of the inner (a) and outer (b) boundary layer profiles at $Re = 1 \times 10^6$ for the natural boundary layers at $x = 0.7$ and 1.9 m as well as the artificially thickened boundary layers for $x = 1.9$ m. The inner boundary layer profiles are compared against the log law (Eq. (4)) where the outer profiles are compared against modified Coles law (Eq. (5)). The profiles are staggered by a $U+$ of 3 in both plots.

3. Results

3.1. Ceiling boundary layer profile

The measured natural and artificially thickened ceiling boundary layer profiles are shown in Fig. 7. Using parameters derived from the natural boundary layers, the inner profiles have been scaled using inner and outer variables and compared to the law of the wall:

$$U^+ = \frac{1}{\kappa} \ln z^+ + A \tag{4}$$

where $U^+ = U/U_\tau$, $z^+ = zU_\tau/\nu$, U is the measured mean velocity and $U_\tau = \sqrt{\tau_w/\rho}$ is the wall friction velocity.

The inner profile can be seen to be linear and closely follows the law of the wall for C_{pi} values ≤ 0.42. As C_{pi} is increased to 0.52, the profile is seen to deviate slightly in the wake region, shifting below the law of the wall. This trend continues as C_{pi} is increased to 0.62 and is an indication of insufficient mixing and profile development between the injection and measurement positions. This is due to the increased boundary layer thickness reducing the development length in terms of number of boundary layer thicknesses (or turnovers), that occur upstream of the measurement position (Belle et al., 2016).

The outer profile is compared against the defect form of the modified Coles law of the wake given by Guo et al. (2005):

$$U^+_\infty - U^+ = -\frac{1}{\kappa}\left(\ln \eta + 2\Pi \cos^2 \frac{\pi\eta}{2} + \frac{1-\eta^3}{3}\right) \tag{5}$$

where $\eta = z/\delta_c$ and δ_c is the boundary layer thickness at which the mean velocity, $U = U_\infty$, which is determined by performing a least squares fit of the outer 0.6δ to Eq. (5). The wake strength factor, Π, was determined using the relationships given by Guo et al. (2005) shown below in Eq. (6) which is based on the measured natural boundary layer properties. This resulted in $\Pi = 0.62$ and was applied to the thickened profiles.

$$\frac{\delta^*}{\delta_c} = \frac{1}{U^+_\infty \kappa}(\Pi + 0.75) \tag{6}$$

The outer profiles show that the natural boundary layers follow the modified Coles law at both streamwise positions closely. In comparison, the artificially thickened boundary layers exhibit a velocity excess in the inner wake region that increases with C_{pi} up to 0.32 where it reaches a maximum. Further increase in C_{pi} sees the velocity excess decrease and remains evident at $C_{pi} = 0.62$. Additionally, the deviations observed in the inner scaled profiles at $C_{pi} = 0.62$ and 0.52 are also evident in the outer profiles manifesting as velocity deficits between z/δ = 0.25 and 0.55.

Performance of the artificially thickening of the boundary layer is also assessed using the thickness and integral properties as a function of C_{pi} (Fig. 8). This is done by normalizing the boundary layer, momentum and displacement thickness by their natural values, δ_N, θ_N and δ^*_N, respectively, at the same location with the results presented in Fig. 8. All

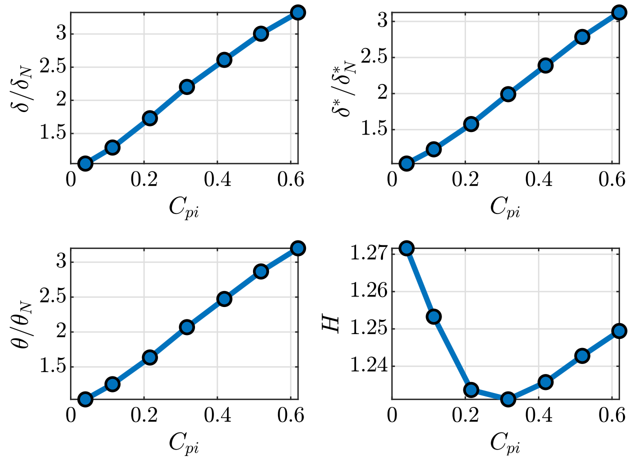

Fig. 8. Variations of thickness and integral properties of the artificially thickened boundary layer.

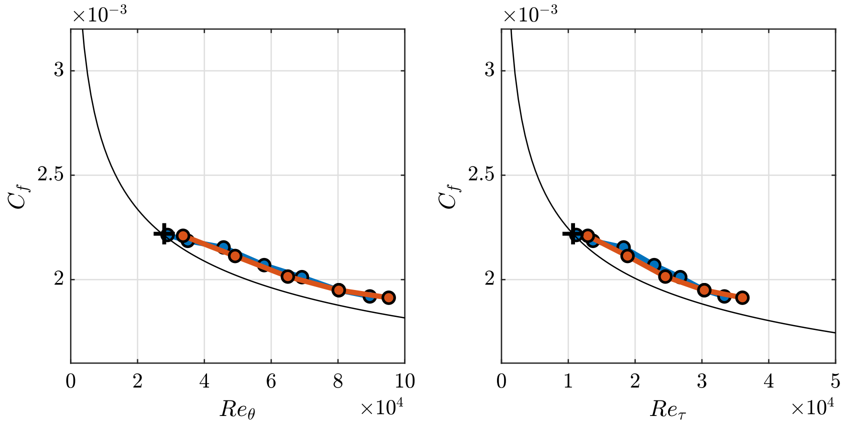

Fig. 9. Comparison of the variation in C_f with Re_θ (left) and Re_τ (right) for the thickened and natural boundary layers. The asymptotic relations of C_f with Re_θ and Re_τ are defined in Eqs. (7) and (8), respectively, and are represented as black lines with the measured natural boundary layer at $x = 1.9$ m represented by a black cross. Measurements taken at a constant C_{pi} are shown in orange with measurements taken a constant Re shown in blue. (For interpretation of the references to colour in this figure legend, the reader is referred to the web version of this article.)

thicknesses show a consistent and steady increase with C_{pi} between 0.1 and 0.5. The shape factor shows good results for all values of C_{pi}, only ranging between 1.23 and 1.27.

To assess the conformity of certain thickened boundary layer properties to those of fully developed flat plate zero pressure gradient boundary layers, asymptotic relations are used. The logarithmic skin friction law described in Jones et al. (2001), Guo et al. (2005), Nagib et al. (2007) provides a relationship between C_f and $Re_\theta = U_\infty\theta/\nu$ and is given as

$$U_\infty^+ = \sqrt{\frac{2}{C_f}} \approx \frac{1}{\kappa}\ln(Re_\theta) + C \tag{7}$$

where C = 5.1 which is derived from a least squares fit of the natural boundary layer. Additionally, a logarithmic relation between $Re_\tau = U_\tau\delta_c/\nu$ and C_f is derived by Guo et al. (2005) and is given as

$$\sqrt{\frac{2}{C_f}} \approx \frac{1}{\kappa_1}\ln(Re_\tau) + B_1 \tag{8}$$

where $\kappa_1 = 0.402$ and $B_1 = 6.94$ are derived from least-squares fitting of the natural boundary layer data. The results presented in Fig. 9 show that the thickened boundary layers show favourable comparison to Eq. (7) for $Re_\theta > 4 \times 10^4$. These results indicate that the boundary layers of $Re_\theta \approx 3 \times 10^4$ and $Re_\tau = 1 \times 10^4$ can be thickened to just below $Re_\theta = 1 \times 10^5$ and $Re_\tau = 4 \times 10^4$, respectively, using this method of artificial thickening. Properties of the natural and artificially thickened boundary layers are summarized in Table 3.

Table 3
Summary of the measured artificial and natural boundary layer properties at $Re = 1 \times 10^6$. All artificially thickened boundary layer measurements were taken at a streamwise position of $x = 1.9$ m.

C_{pi}	δ (mm)	δ^* (mm)	θ (mm)	H	Re_θ	Re_τ	C_f
Artificial							
0.04	33.8	4.45	3.50	1.27	28,971	11,197	0.0022
0.11	41.6	5.31	4.24	1.25	35,034	13,699	0.0022
0.22	55.9	6.82	5.53	1.23	45,746	18,280	0.0022
0.32	71.1	8.62	7.00	1.23	57,896	22,855	0.0021
0.42	84.3	10.34	8.37	1.24	69,204	26,753	0.0020
0.52	97.1	12.06	9.70	1.24	80,241	30,360	0.0019
0.62	107.4	13.52	10.82	1.25	89,523	33,365	0.0019
Natural							
$x = 0.7$ m	19.1	2.59	2.04	1.28	17,601	6,681	0.0024
$x = 1.9$ m	32.3	4.22	3.38	1.28	27,987	10,712	0.0022

Comparing results with those provided by Belle et al. (2016) highlights the improved artificially thickened boundary layer properties of the redesigned thickening plate. The outer velocity profiles are shown to be as accurate, if not more accurate than the ones produced by previous designs for a much wider range of C_{pi}. With the large open area of the plate, this allowed relatively larger boundary layer thicknesses to be generated without sacrificing profile accuracy and allowing a larger range of immersion ratios to be investigated. Integral properties and asymptotic relations of the redesigned plate reinforce the conformity of the artificially thickened boundary layers to those developed on a flat plate in a zero pressure gradient.

3.2. Steady and unsteady forces

3.2.1. Effect of Reynolds number

The effect of Re on the steady normal force acting on a hydrofoil in low and high boundary layer immersion situations is presented in Figs. 10 and 11, respectively. First analysing the low-immersion case, the 240 mm hydrofoil is partially immersed in a relatively thin natural boundary layer resulting in an immersion ratio, δ/b, of approximately 0.08. As α is increased from 0°, all Re cases are seen to exhibit a steady increase in C_N before deviating from the linear trend with an increase in the normal force gradient highlighted in the $\partial C_N/\partial\alpha$ plot (Fig. 10). This deviation first occurs for $Re = 0.4 \times 10^6$ at $\alpha \approx 2.5°$ followed by the remaining cases in quick succession in order of ascending Re. As α is increased further, the $\partial C_N/\partial\alpha$ reaches a maximum with all Re cases $\leq 1.0 \times 10^6$ decreasing by $\alpha = 10°$. This increase in $\partial C_N/\partial\alpha$ for $Re = 0.4 \times 10^6$ corresponds with a local increase in the unsteadiness shown in C_N'.

This C_N deviation and unsteadiness behaviour is similar to that observed when a laminar separation bubble (LSB) forms on a hydrofoil. The adverse pressure gradient causes the laminar flow to separate and quickly transition to turbulent flow (Lissaman, 1983) before reattaching further downstream and forming a region of re-circulating flow known as a laminar separation bubble (Hoerner and Borst, 1985). At lower incidences where the adverse pressure gradient is low, a relatively large LSB can form between mid-chord and the trailing edge of the hydrofoil. This relatively large LSB has the ability to induce fluctuations such as those observed at $\alpha \approx 5.5°$ in Fig. 10. As the incidence increases to 7°, the resulting change in the suction side pressure distribution has been shown to cause the LSB to shrink and shift towards the leading edge (Hoerner and Borst, 1985). This has the effect of increasing the effective camber of the hydrofoil (Hansen et al., 2014) and thereby increasing the C_N and potentially causing the previously mentioned deviation. This deviation observed in current C_N results, potentially due to an LSB, exhibits a Re dependence with the deviation occurring at a higher incidence for higher Re. This has previously been attributed to the increased resistance to separation a higher Re flow provides where the flow over the hydrofoil would require an increased adverse pressure gradient to separate, which does not occur until higher incidences (Swalwell et al., 2001).

As α increases past 10°, $\partial C_N/\partial\alpha$ continues to reduce before levelling out as the hydrofoil approaches stall with the $Re = 0.4 \times 10^6$ case stalling first at $\alpha = 16°$. The other Re cases stall soon after in order of ascending Re with the $Re = 1.2 \times 10^6$ case being the last to stall at 17°. The sudden drop in C_N is an indication of leading-edge type stall similar to that observed when a short LSB bursts (Hoerner and Borst, 1985). Stall due to a short LSB bursting occurs when the increased adverse pressure gradient from the increasing incidence strains a short LSB to the point the separated flow is unable to reattach to the hydrofoil (Hoerner and Borst, 1985). This results in separated flow covering the majority of the hydrofoils suction side and causing a sudden drop in the normal force and rise in unsteadiness as observed in Fig. 10. Stall is delayed with increasing Re as the increased kinetic energy of the higher Re flow is more resistant to separation.

It is worth noting the changes in the hysteresis characteristics between the Re cases. For the low-immersion case in Fig. 10, the width of the C_N hysteresis loop is seen to increase with Re from approximately 3.0° at $Re = 0.4 \times 10^6$ to 5.5° at $Re = 1.0 \times 10^6$, similar to that observed by Timmer (2008). The hysteresis behaviour is discussed further in Section 3.2.2 where the role of boundary layer immersion is considered.

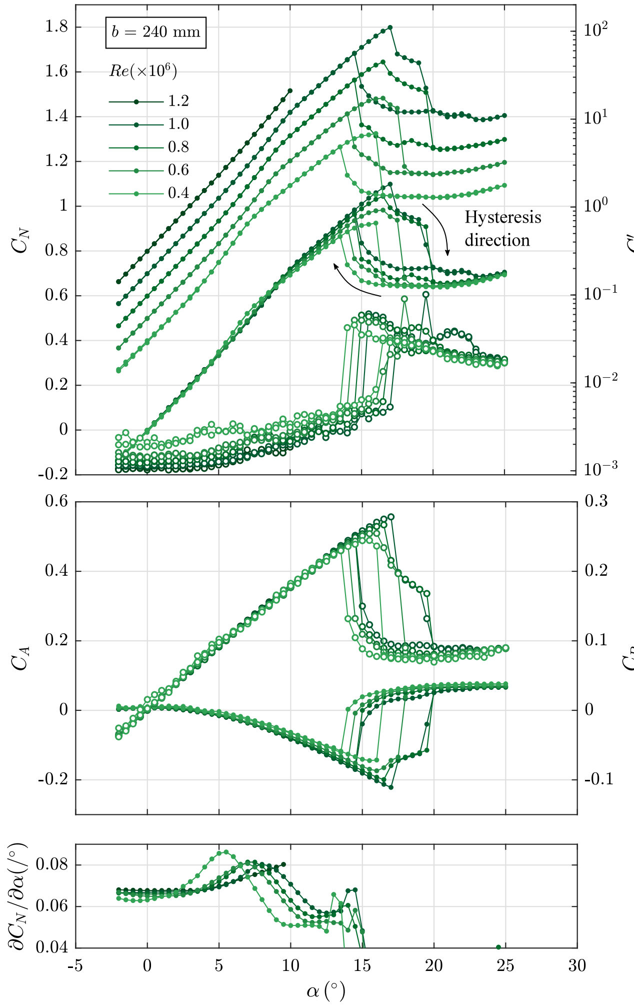

Fig. 10. Mean (•) and standard deviation (○) of the time-varying normal force, C_N and C'_N respectively, with incidence, α, acting on the 240 mm span hydrofoil for different free-stream velocities showing the influence of Re (top). The hydrofoil is immersed in the natural boundary layer, resulting in an immersion ratio, δ/b, of 0.08. C_N is plotted twice with the second plotted with an initial C_N offset of 0.4 for $Re = 0.4 \times 10^6$ and then staggered by 0.1 with increasing Re. Mean of C_A (•) and C_P (○) for varying incidences (middle) provides insight into the mechanics of the excitations. The normal force slope, $\partial C_N/\partial\alpha$, is used to highlight trends in the normal force behaviour (bottom).

Comparing the C_N behaviour of the 240 mm hydrofoil low-immersion case to the 120 mm hydrofoil high-immersion case, i.e. the two extremes, for various Re reveals some interesting differences. In the high-immersion case, the 120 mm hydrofoil is immersed in the thickest artificially thickened boundary layer resulting in a $\delta/b = 0.81$ with the forces acting on the hydrofoil for various Re presented in Fig. 11. As α is increased from 0°, all Re cases exhibit a similar $\partial C_N/\partial\alpha$ up to 10°. Compared to the low-immersion case, the high-immersion case exhibits a lower $\partial C_N/\partial\alpha$, attributed to lower aspect ratio and increased exposure to lower momentum flow of the ceiling boundary layer. Additionally, the high-immersion case exhibits no indication of LSB formation for any of Re case unlike that observed in the low-immersion case. This may be attributed to the transfer of momentum and TKE from the encountered ceiling boundary layer to the one developing over the hydrofoil. This transfer of TKE energizes the boundary layer developing over the hydrofoil, promoting earlier transition to the turbulent regime, increasing its resistance to separation (Hoffmann and Kassir, 1988) and thereby preventing LSB formation.

Increasing the incidence past 10° sees a gradual reduction in the normal force gradient in the high-immersion cases. This behaviour is shown to have a Re dependence with the reduction in $\partial C_N/\partial\alpha$ occurring first in the $Re = 0.4 \times 10^6$ case at $\alpha \approx 10°$, followed by the other Re cases in ascending order. Further increase in incidence sees the Re cases approach stall with the $Re = 0.4 \times 10^6$ case stalling first at $\alpha = 21.5°$ with the remaining Re cases stalling in succession in ascending order with all cases stalled by $\alpha = 26°$. The gradual stall behaviour observed in the high-immersion case is typical of the trailing-edge type where the flow starts to separate close to the trailing-edge with the separation point migrating

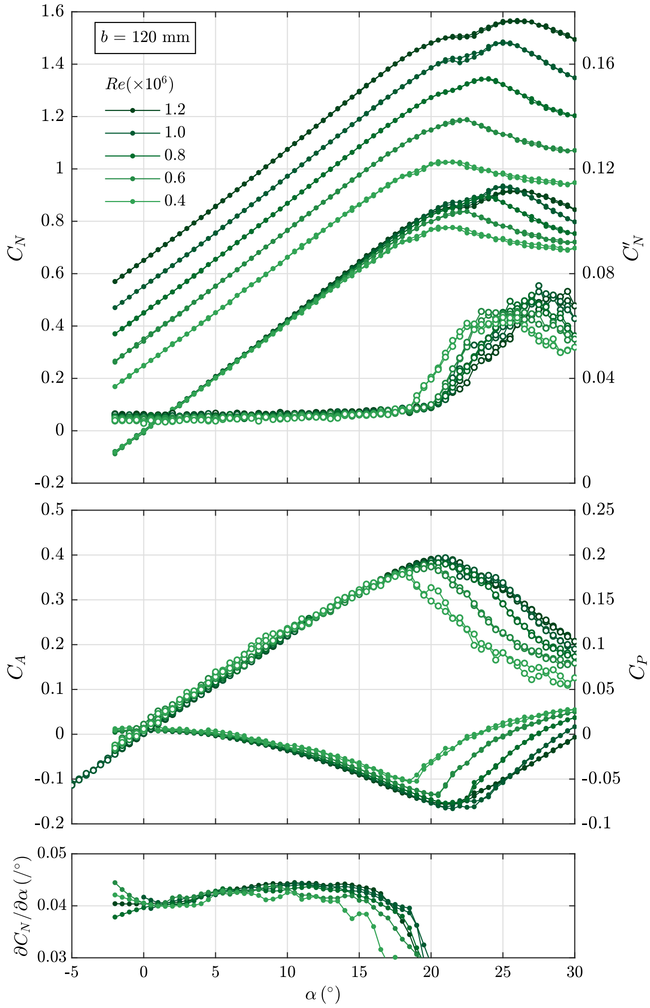

Fig. 11. Mean (•) and standard deviation (∘) of the time-varying normal force, C_N and C_N' respectively, with incidence, α, acting on the 120 mm span hydrofoil for different free-stream velocities showing the influence of *Re* (top). The hydrofoil is immersed in an artificially thickened boundary layer where $\delta/b = 0.81$. The C_N data is also replotted to provide clarity of the individual curves with an initial C_N offset of 0.4 for $Re = 0.4 \times 10^6$ and then staggered by 0.1 with increasing *Re*. Mean of C_A (•) and C_P (∘) for varying incidences (middle) provides insight into the mechanics of the excitations. The normal force slope, $\partial C_N/\partial\alpha$, is used to highlight trends in the normal force behaviour (bottom).

upstream as α increases. This differs to the sudden leading-edge type stall observed in the low-immersion case with the difference attributable to the increased transfer of TKE and momentum as well as the reduced aspect ratio.

3.2.2. Effect of boundary layer immersion

A comparison of the C_N behaviour for a range of δ/b acting on the 120 mm and 240 mm span hydrofoils (for $Re = 1.0 \times 10^6$) is presented in Figs. 12 and 13, respectively. In both cases, C_N decreases as δ/b increases for all pre-stall α. This is due to the increased span that is subjected to the lower momentum flow within the ceiling boundary layer resulting in a reduction in normal force. In addition, step increases to the level of unsteadiness can be observed with C_N' increasing incrementally with δ/b at all pre-stall α. This can be attributed to the increased exposure of the hydrofoils to the turbulent flow within the ceiling boundary layer and ceiling-junction horseshoe vortex as δ is increased. The flow at the ceiling-junction is characterized by a horseshoe vortex that forms at the leading edge and wraps around the wing with the turbulence in the vicinity of the vortex remaining high (Awasthi et al., 2020).

On the 120 mm hydrofoil, there are indications of an LSB forming with a deviation evident in $\partial C_N/\partial\alpha$ at $\alpha \approx 11°$ for the lower immersion ratio cases that disappears as the boundary layer thickens (Fig. 12). This trait is more evident on the 240 mm hydrofoil in Fig. 13 and can potentially be attributed to the shrinking of the LSB either in the chordwise direction, spanwise direction or both. As mentioned earlier in Section 3.2.1, the behaviour of the LSB is influenced by the transfer of TKE and momentum (Hoffmann and Kassir, 1988) which would increase with increased immersion in the ceiling boundary layer. In regards to the chordwise length of the LSB, this transfer of TKE and momentum promotes earlier

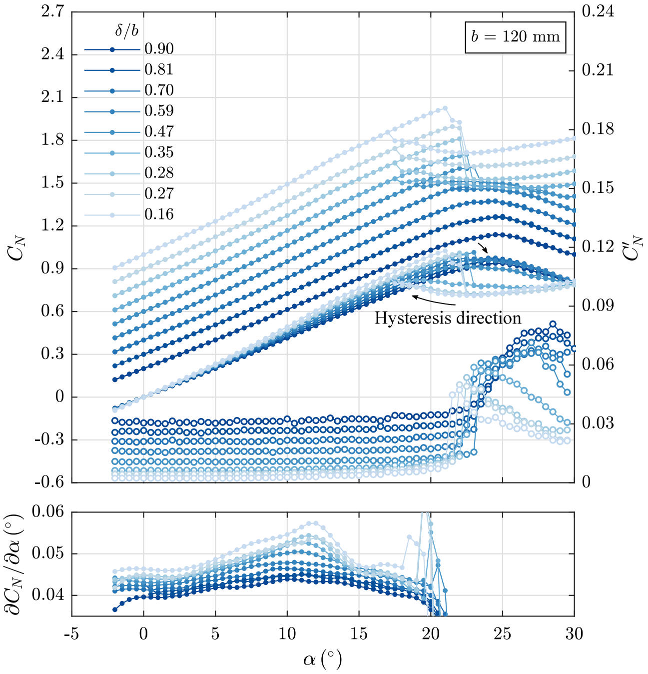

Fig. 12. Mean (•) and standard deviation (∘) of the time-varying normal force, C_N and C_N' respectively, with incidence, acting on the 120 mm span hydrofoil for δ/b ranging from 0.16 to 0.90 (top). The C_N data is also replotted to provide clarity of the individual curves with an initial C_N offset of 0.2 and then staggered in 0.1 increments for each δ/b case. Characteristics in the C_N behaviour for varying α is highlighted in the $\partial C_N/\partial\alpha$ plot (bottom) which is passed through a Savitsky–Golay filter of the 2nd order to smooth out the data.

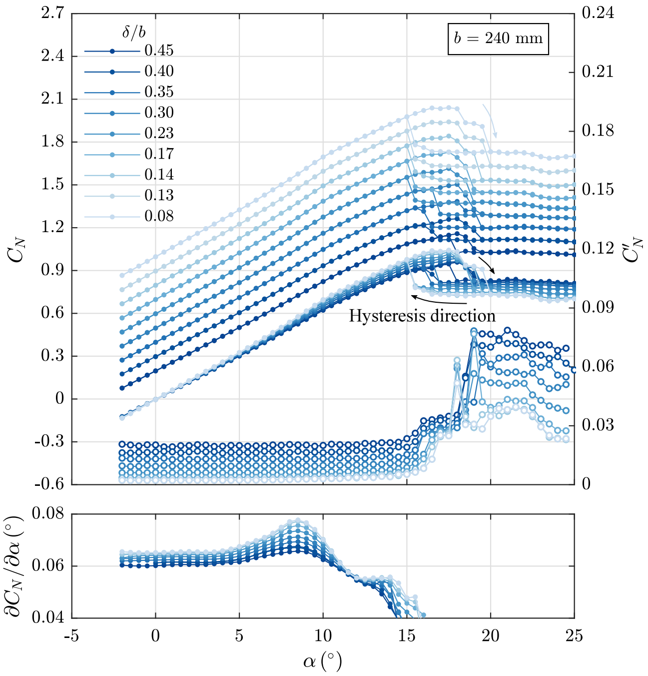

Fig. 13. Mean (•) and standard deviation (∘) of the time-varying normal force, C_N and C_N' respectively, with incidence, acting on the 240 mm span hydrofoil for δ/b ranging from 0.08 to 0.45 (top). The C_N data is also replotted to provide clarity of the individual curves with an initial C_N offset of 0.2 and then staggered in 0.1 increments for each δ/b case. Characteristics in the C_N behaviour for varying α is highlighted in the $\partial C_N/\partial\alpha$ plot (bottom) which is passed through a Savitsky–Golay filter of the 2nd order to smooth out the data.

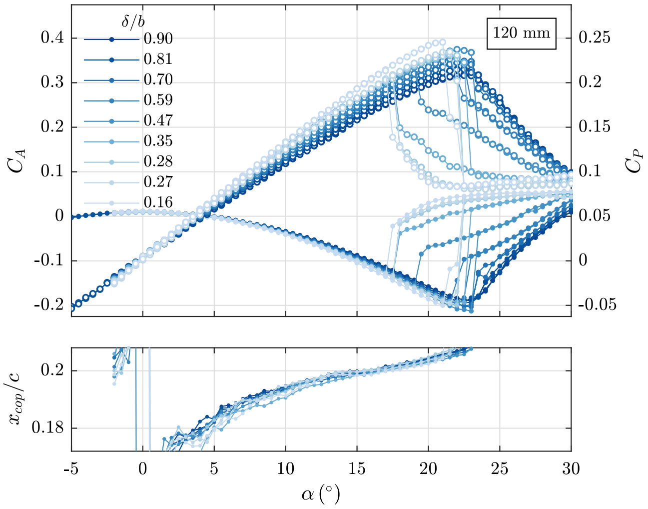

Fig. 14. Mean of C_A (•) and C_P (∘) with varying incidence (top) acting on the 120 mm hydrofoil for δ/b ranging from 0.16 to 0.90 provides insight into the mechanics of the excitations. Behaviour of x_{cop}/c with varying α (bottom) shows how increasing immersion shifts the centre of pressure along the chord.

transition of the separated flow encouraging reattachment closer to the leading edge, shrinking the chordwise length of the LSB and therefore its influence on the C_N force generated. In regards to the spanwise length of the LSB, sufficient transfer of TKE and momentum to the early stages of the hydrofoil boundary layer could cause it to transition before reaching the maximum adverse pressure gradient, giving it the ability to resist separation, preventing an LSB from forming. This would result in LSB formation only being suppressed in the spanwise portion of the hydrofoil that is immersed in the ceiling boundary layer. This would result in the LSB influence decreasing with increased immersion on parameters such as the deviation in $\partial C_N/\partial\alpha$. The relative amplitude of the $\partial C_N/\partial\alpha$ peak decreasing with increasing immersion is seen to disappear by $\delta/b \geq 0.59$ with little non-linearity in the normal force gradient at pre-stall incidences, suggesting an LSB no longer forms on the hydrofoil (Fig. 12).

Similar behaviour is observed in C_A and C_P (Figs. 14 and 15) as seen with C_N where the absolute of each force decreases steadily with increased immersion in the boundary layer. Utilizing C_N and C_P to determine the x_{cop} provides insight into how boundary layer immersion influences the pressure distribution over the suction side of the hydrofoil. Upon initial comparison of the two hydrofoils (Figs. 14 and 15), it is revealed that x_{cop}/c shifts further along the 120 mm hydrofoil moving steadily towards the trailing edge with increasing incidence. x_{cop}/c is observed only to shift from $x_{cop}/c \approx 0.23$ at $\alpha = 5°$ to $x_{cop}/c \approx 0.25$ at $\alpha = 10°$ where it remains in the same position up to $\alpha = 15°$ for all δ/b. This *'shoulder'* can partially be seen on the 120 mm hydrofoil at low δ/b suggesting it is affected by the presence of an LSB.

Furthermore, the increased immersion of the 120 mm hydrofoil within the ceiling boundary layer is observed to have significant influence on the stall characteristics (Fig. 12). At low-immersion ratios, $\delta/b \leq 0.47$, stall is sudden with C_N dropping significantly at $\alpha = 21.0°$ for $\delta/b = 0.16$ to $\alpha = 23.0°$ for $\delta/b = 0.47$. As mentioned previously, this is typical of leading-edge type stall where the LSB *'bursts'* as the separated flow is unable to reattach with an increase in α. This results in separated flow covering the majority of the chord causing a sudden drop in C_N and a jump in C_N'. As δ/b is increased to 0.59, the hydrofoil is seen to exhibit a gradual drop in C_N as the hydrofoil stalls at $\alpha = 23.5°$, typical of trailing-edge stall (Hoerner and Borst, 1985). This transition from leading-edge to trailing-edge type stall as δ/b is increased from 0.47 to 0.59 also coincides with the disappearance of the deviation in the normal force curve attributed to the LSB. Further increases in δ/b sees stall become more gradual as well as being delayed, again attributable to the increased transfer of TKE. With the increased TKE, the hydrofoil boundary layer can resist separation, preventing leading-edge type stall and delaying trailing-edge type stall.

As mentioned previously in Section 3.2.1, the width of the C_N hysteresis loop is shown to increase with *Re* for the low-immersion case ($\delta/b = 0.08$) in Fig. 10. Analysing the influence of boundary layer immersion on the hysteresis behaviour in Fig. 13, it is observed that increased immersion reduces the hysteresis loop width from 5.0° at $\delta/b = 0.08$ to 2.0° at $\delta/b = 0.45$ This hysteresis loop width variation is primarily attributed to changes in the stall incidence with little variation in the incidence that the flow reattaches.

3.3. Force spectra

To allow unsteady loading characteristics to be identified, spectra have been obtained from the time series of the normal force and presented non-dimensionally as C_N in the form of power spectral density (PSD), with reduced frequency,

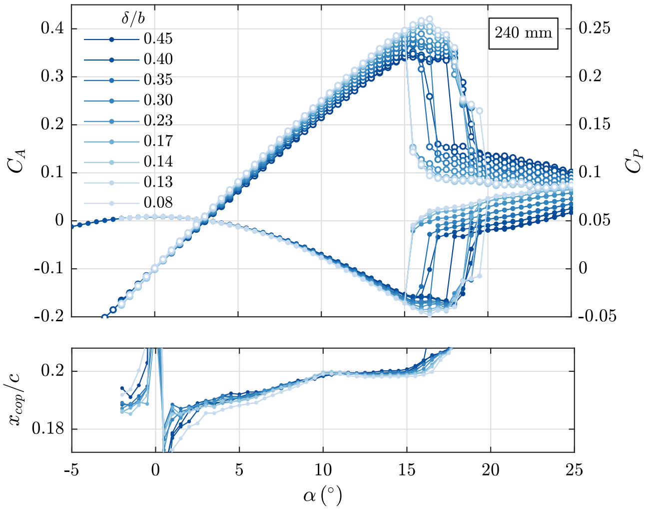

Fig. 15. Mean of C_A (•) and C_P (○) with varying incidence (top) acting on the 240 mm hydrofoil for δ/b ranging from 0.08 to 0.45 provides insight into the mechanics of the excitations. Behaviour of x_{cop}/c with varying α (bottom) shows how increasing immersion shifts the centre of pressure along the chord.

$f' = fc/U_\infty$. Peak frequencies are present in all spectra due to the frequency response of the coupled force balance and hydrofoil system. The natural frequencies of the hydrofoils are clearly evident in the C_N spectra with peaks occurring at the reduced frequency equivalents of the modes stated in Table 1. Variation between the estimated (Table 1) and measured modal frequencies can be attributed to the simplification of a rectangular plate in added mass calculations and a low aspect ratio planform where 3D effects are more pronounced. Due to this inherent dynamic response from the coupled balance/hydrofoil system, the resolvable frequency range for the present measurements extends to about 250 and 60 Hz for the 120 and 240 mm span hydrofoils, respectively. This equates to an f' for the 120 and 240 mm hydrofoils of 0.9 & 2.0 for $Re = 1.0 \times 10^6$, and 4.0 & 4.5 at $Re = 0.4 \times 10^6$, respectively. Effective reduction of electrical noise contamination in the spectra was achieved using the modified IOP method as described in Section 2.6. However, power supply odd harmonics are still partially evident in the spectra, along with by-products of the modified IOP method, appearing as tonal low amplitude peaks and troughs.

3.3.1. Effect of incidence

The effect of incidence on the C_N spectra for both hydrofoils is highlighted in Fig. 16 for Re ranging from 0.2×10^6 to 1.2×10^6. In the low-immersion cases where the 240 mm span hydrofoil is partially immersed in a thin boundary layer with $\delta/b = 0.06$, the pre-stall incidences exhibit a relatively uniform power distribution at all Re in the resolvable frequency range. Increases in α from 0° to 5° and then to 10° causes broadband excitation in the C_N spectra within an order of magnitude. This broadband excitation at pre-stall incidences is potentially due to self-generated turbulence of the hydrofoil. The increase in power with incidence does reduce with increasing f' presumably due to spatial filtering where turbulence spatial scales are much smaller than the hydrofoil chord.

Analysis of the spectra at higher incidences shows that when α is increased sufficiently, there is a large jump in power of 3 to 4 orders of magnitude, particularly at low f'. This jump in power coincides with the hydrofoil stalling for all Re as shown in the steady C_N forces in Fig. 10. With this jump in power characterized particularly by increases predominately at low f' suggests the sudden leading-edge type stall is associated with large-scale low-frequency excitations. Additionally, each of the stalled spectra are observed to exhibit a frequency band where the C_N power remains constant. The limits of the frequency band vary between incidences occurring around $0.07 \leq f' \leq 0.2$.

Changes in spectral features as α is varied are observed to be less pronounced in the high-immersion case ($\delta/b = 0.83$) with variation more gradual between incidences compared with those observed in the low-immersion case with $\delta/b = 0.06$ (Fig. 16). This indicates immersion in the ceiling boundary layer tends to homogenize the unsteady flow resulting in a broadband range of disturbances as opposed to more defined and tonal disturbances that would result in a more pronounced spectral features as evident in the low-immersion cases. C_N power at all incidences eventually collapse to the $\alpha = 0°$ case beyond a certain frequency, which increases with α in all Re cases, and all spectra converge by $f' = 0.4$. In other words, increases in incidence are shown to have significant effect at low frequencies, the frequency range of which increases with incidence up to a reduced frequency of about 0.4. Beyond $f' = 0.4$, incidence changes have negligible effect. Over this region, the unsteadiness is entirely due to the wall boundary layer with a constant roll-off slope of -3.

Furthermore, the high-immersion cases exhibit a broadband peak at $f' \approx 0.2$ in which the peak amplitude does not vary with α. This peak becomes lost at high α in the broadband C_N excitation from the self-generated turbulence of the

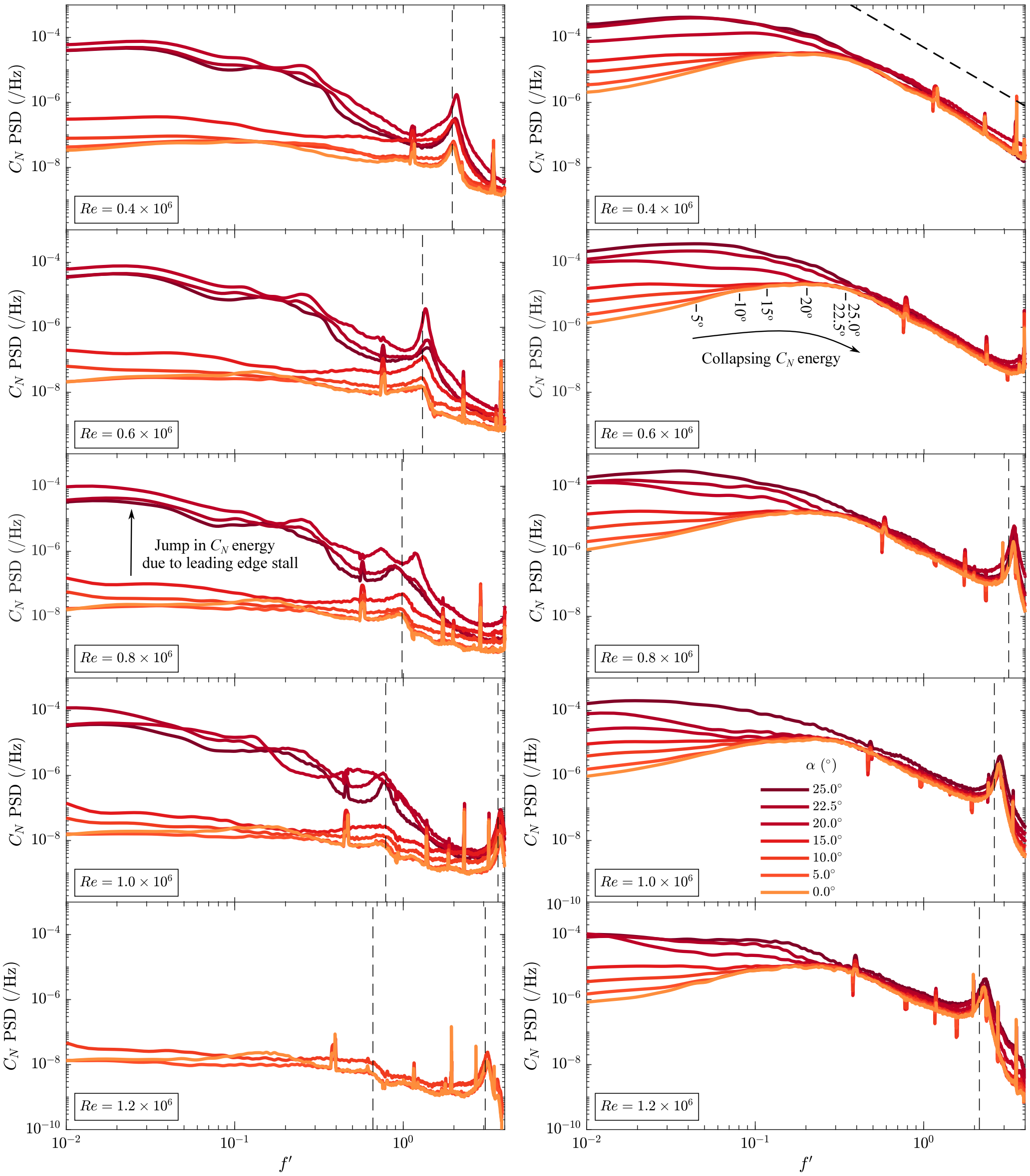

Fig. 16. Spectra of C_N highlighting the influence of α at multiple Re for the 240 mm span hydrofoil in a thin boundary, $\delta/b = 0.06$, (left) and the 120 mm span hydrofoil in a artificially thick boundary layer, $\delta/b = 0.83$, (right). The non-dimensional natural frequency of the hydrofoils (vertical dashed line) have significant effect on the loading spectra, particularly the 240 mm hydrofoil. A $f'^{(-3)}$ reference for the slope of the roll-off is provided in the 120 mm hydrofoil spectra at $Re = 0.4 \times 10^6$ (diagonal dashed line).

hydrofoil. With the broadband peak not evident in the low-immersion case and not varying with α or Re, results suggest the disturbance is due to the ceiling boundary layer which is discussed further later.

There are indications of vortex-induced vibrations (VIV) in the C_N spectra for both the 240 mm hydrofoil in a thin boundary layer and 120 mm hydrofoil in a thick boundary layer (Fig. 16). Both hydrofoils are subjected to a range of disturbances depending on the conditions with potential excitations including transition instabilities and coherent shedding from the leading edge. The amplitude of the peak attributed to the resonant response of the hydrofoil is seen to exhibit significant amplification depending on the incidence and Re. This suggests excitations are inducing VIV that would result in increased C_N spectral levels. When comparing the C_N spectra for the 240 mm hydrofoil in a thin boundary layer to that of the 120 mm hydrofoil in a thick boundary layer, the resonant response is significantly different. The C_N power of the resonant response for the low-immersion case shows amplification with decreasing Re and increasing α, particularly at stall incidences (Fig. 17). In comparison, the high-immersion case at all Re shows minimal increase with α. This suggests that for the high-immersion case there is no substantial vortex shedding at the resonant frequency that would cause significant VIV.

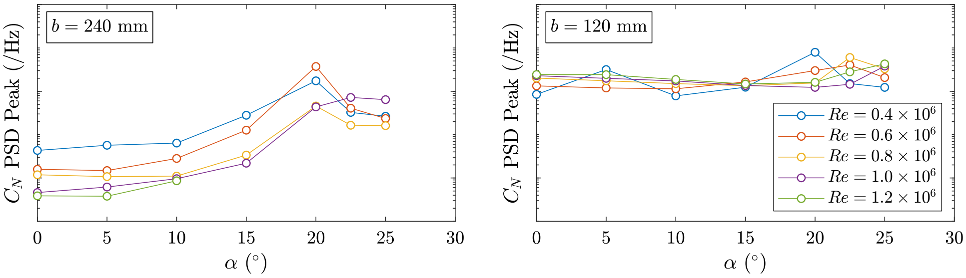

Fig. 17. Peak C_N PSD values for resonant response of the 240 mm (left) and 120 mm (right) hydrofoils in relatively thin and thick boundary layers, respectively.

3.3.2. Effect of Reynolds number

The effect of Re on the unsteady loading experienced by the hydrofoils in both low and high-immersion cases is shown in Fig. 18. For the low-immersion case where $\delta/b = 0.06$, the lowest Re case ($Re = 0.4 \times 10^6$) exhibits the highest C_N power in the resolvable frequency range for pre-stall incidences, $\alpha \leq 15°$. For all Re cases there is a general decrease in the normal-force power across the measured frequency range with increased Re.

At $\alpha = 5°$ in the low-immersion case, the $Re = 0.4 \times 10^6$ data shows significantly higher broadband energy levels compared to the other cases. As indicated in Fig. 11, the formation of an LSB is inferred, a known source of vortex shedding and hence, unsteady loading (Baragona et al., 2003). High-speed flow visualization and velocity measurements by Kirk and Yarusevych (2017) have shown coherent structures associated with the LSB occur at reduced frequencies ranging from 0.89 to 6.37, depending on incidence. This has the potential to cause vortex induced vibration at the same frequency as the natural frequency of the hydrofoil which occurs at $f' \approx 2.0$ for $Re = 0.4 \times 10^6$. This would lead to resonance that could cause amplification in the response such as that observed in the C_N spectra of the 240 mm hydrofoil where the magnitude is shown to increase with both incidence and Re. In contrast, the 120 mm hydrofoil highly immersed showed no variation in the amplitude of the resonant peak with incidence or Re. Further investigation with coupled flow measurements are required to determine the source of these excitations.

Increasing α from 5° to 15° results in a small increase in C_N broadband energy with the hydrofoil still at a pre-stall incidence. Further increase in α to 20° sees a sudden increase in C_N energy, particularly at low f' as the hydrofoil experiences stall (Fig. 11), characterized by separation from the leading edge. As mentioned previously in Section 3.3.1, vortex shedding at stall can lead to VIV, resulting in amplification of the hydrofoil resonant response as observed at $Re = 0.4$ and 0.6×10^6 for $\alpha = 20°$. At $\alpha = 25°$, all Re cases are experiencing stall with separation along the full chord of the hydrofoil. The C_N spectra are seen to exhibit similar trends for $f' \leq 0.8$ with all Re cases exhibiting multiple '*shoulders*' at $f' \approx 0.18$ and 0.34 with matching roll-off rates. These '*shoulders*' indicate the presence of coherent structures shedding off the hydrofoil due to the separated flow indicative of shedding leading-edge structures. These results provide insight into the range of frequencies and hence size distribution in the wall boundary layer that affect the unsteady loading of the hydrofoil. Based on the observed f', it is unlikely that these are due to the shedding of roll-up vortices which are observed to occur around $f' \geq 1.5$. These excitation occur at a much lower frequency closer to that observed of wake vortex shedding (Yarusevych et al., 2009). However, further insight into the phenomena involved through flow measurements is required to identify the physics responsible for the excitations.

The high-immersion cases where $\delta/b = 0.83$ exhibit different trends to those observed in the low-immersion case as well as similarities. At $\alpha = 0°$, the C_N energy is seen to increase steadily as Re decreases, similar to that observed in the low-immersion cases. Increased immersion and exposure to the embedded turbulence of the ceiling boundary layer results in a broadband increase in C_N energy. The increased immersion is also seen to result in a broadband peak at $f' \approx 0.2$ for all Re which is not observed in the low-immersion cases. As f' increases past 1, the energy levels are seen to converge due to varying roll-off rates between the different Re cases.

Increasing the incidence to 5° sees minimal change in the C_N spectra for all Re, unlike that observed in the low-immersion case. This is attributed to the encountered ceiling boundary layer preventing an LSB from forming on the hydrofoil and causing unsteady loading. As α is increased to 15°, a rise in low-frequency C_N energy is evident for all Re cases. This sees the $f' \approx 0.2$ peak begin to diminish in the power rise attributable to self-generated turbulence of the hydrofoil from separation at the trailing edge.

Re is shown to alter the stall behaviour of the hydrofoil with stall being delayed and max C_N being increased with rising Re, particularly in the high-immersion case (Fig. 11). At an incidence of 20°, the unsteady loading characteristics at various stages of stall is captured by the 5 Re cases. At relatively low speeds with $Re = 0.4 \times 10^6$, the hydrofoil is close to max C_N at 20° with the C_N spectra showing high energy at low f'. This increased low f' excitation sees the broadband peak at $f' \approx 0.2$ disappear with a plateau in the spectra forming for frequencies up to $f' \approx 0.1$ before rolling off. For $Re = 0.6 - 0.8 \times 10^6$, the hydrofoil is at a pre-stall incidence at 20° but would still be experiencing separation for a large portion of the chord that would cause substantial unsteady loading. The reduced excitation sees evidence of the

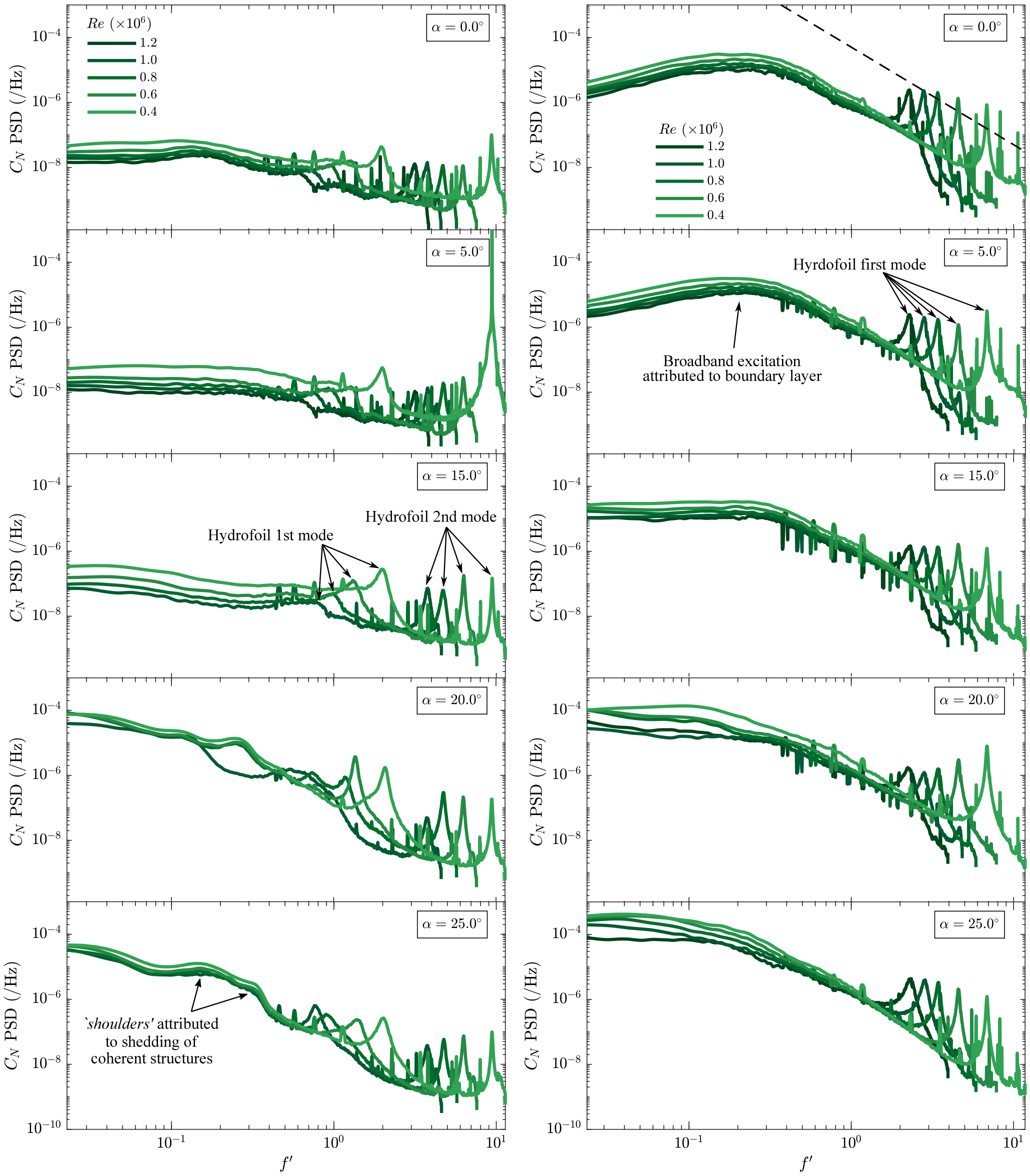

Fig. 18. Spectra of C_N highlighting the influence of *Re* at multiple α for the 240 mm span hydrofoil in a thin boundary, $\delta/b = 0.06$, (left) and the 120 mm span hydrofoil in a artificially thick boundary layer, $\delta/b = 0.83$, (right). The non-dimensional natural frequency of the hydrofoils (vertical dashed line) have significant effect on the loading spectra, particularly the 240 mm hydrofoil. A $f'^{(-3)}$ reference for the slope of the roll-off is provided in the 120 mm hydrofoil spectra at $\alpha = 0°$ (diagonal dashed line).

broadband peak at $f' \approx 0.2$ as well as the 'shoulder' at $f' \approx 0.1$ observed at $Re = 0.4 \times 10^6$. This indicates that the broadband peak at $f' \approx 0.2$ is associated with the encountered ceiling boundary layer where the peak at 0.1 is associated with self-generated turbulence from the hydrofoil stalling.

3.3.3. Effect of boundary layer immersion

The effect of boundary layer immersion on the unsteady loading of the 120 mm and 240 mm hydrofoil is both complex and broad as shown in Fig. 19. At an incidence of 0° where self-generated turbulence of the hydrofoil is at a minimum, the direct influence of the encountered ceiling boundary layer is highlighted. Both hydrofoils are seen to experience an incremental increase in energy across the entire frequency range with increased δ/b. The primary feature in the spectra of both hydrofoils is the previously mentioned broadband peak at $f' \approx 0.2$ which is shown to increase in relative amplitude with δ/b. An exception to this is the lowest immersion case which instead exhibits a more defined peak at $f' \approx 0.13$ on both hydrofoils. Additionally, the roll-off slope past the $f' \approx 0.2$ broadband peak is observed to increase with δ/b.

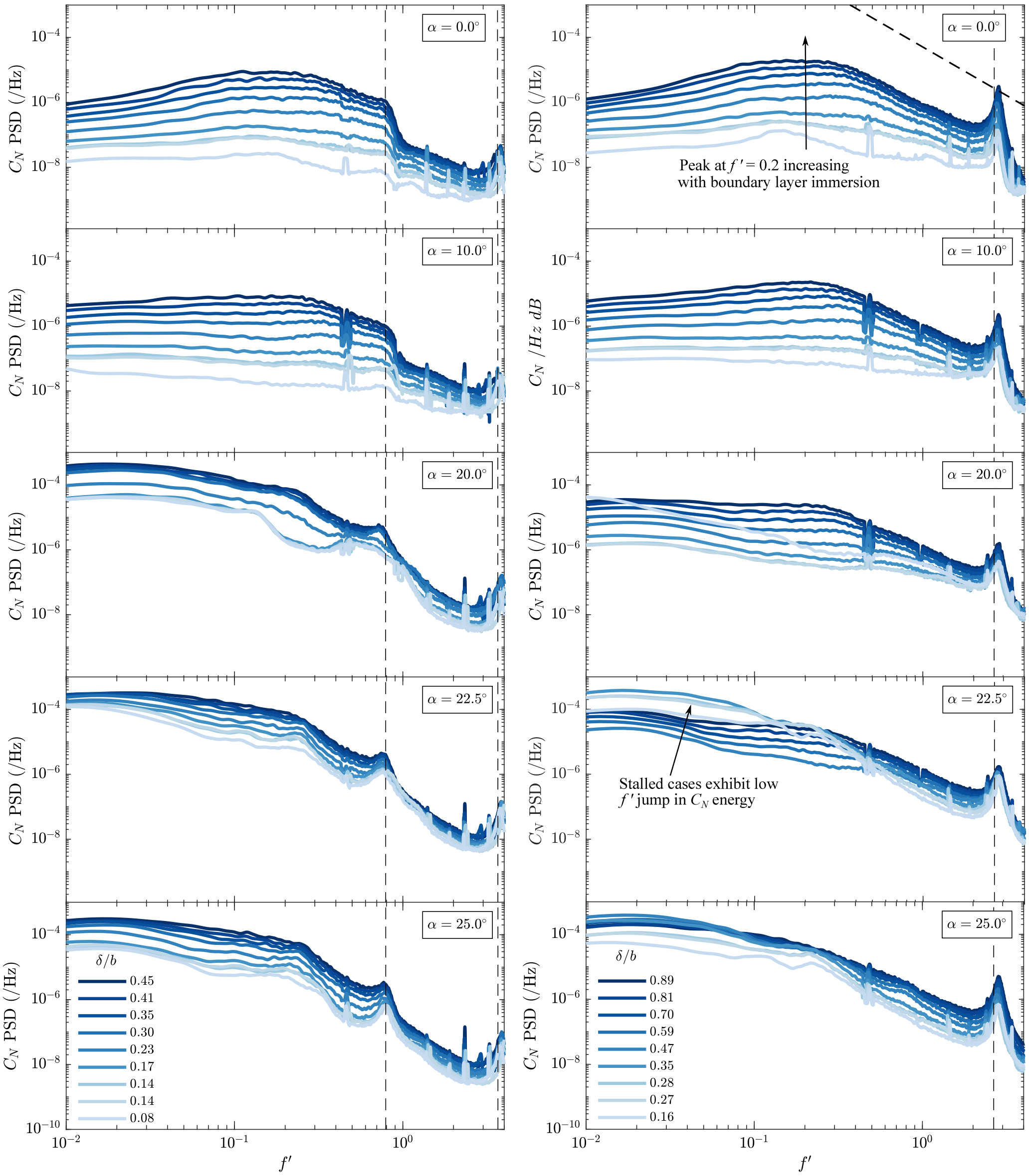

Fig. 19. Spectra of C_N highlighting the influence of the level of boundary layer immersion at various α for the 240 mm (left) and 120 mm (right) hydrofoils at $Re = 1.0 \times 10^6$. The non-dimensional natural frequency of the hydrofoils (vertical dashed line) have significant effect on the loading spectra, particularly the 240 mm hydrofoil. A $f'^{(-3)}$ reference for the slope of the roll-off is provided in the 120 mm hydrofoil spectra at $\alpha = 0°$ (diagonal dashed line).

Behaviour of the broadband peak at $f' \approx 0.2$ increasing in relative magnitude with δ/b suggests the excitation is due to coherent structures within the ceiling boundary layer. Occurring at a consistent f', the coherent structures must have a compatible length scale and advection velocity that results in an excitation at a reduced frequency of approximately 0.2 at all boundary layer thicknesses. Experiments conducted by Hutchins and Marusic (2007) revealed inner and outer energy peaks in one-dimensional streamwise pre-multiplied spectra of a turbulent boundary layer. The outer energy peak was characterized by coherent structures, referred to as *'superstructures'*, with a consistent length scale, λ_x, of 6δ and outer coordinates of $z/\delta \approx 0.06$. Unfortunately, the advection speed of the these *'superstructures'* are difficult to measure experimentally. However, results from boundary layer simulations conducted by Del Álamo and Jiménez (2009) indicated the larger *'global'* modes travel at a speed proportional to the bulk velocity as opposed to the local mean velocity in the boundary layer. Based on a length scale of 6δ and assuming the advection velocity is sufficiently close to the free-stream, i.e. $U_x = U_\infty$, this would result in $f' \approx 0.156$ for the largest boundary layer. This is relatively close considering the broadband nature of the peak suggesting it could be the potential cause of the excitation. However, without flow measurements to provide sufficient insight into the phenomena involved, the cause of the broadband excitation cannot be identified.

Closer inspection of the 120 mm high δ/b spectra at 0° reveals a '*shoulder*' in the broadband peak where the C_N power starts to roll-off, known as the cut-off frequency. The cut-off frequency can be seen to decrease as δ/b increases. Furthermore, the rate of decay in the C_N power past the cut-off frequency, known as the roll-off, can be seen to vary between δ/b cases with the roll-off increasing with δ/b. This provides insight into the size distribution of the eddies encountered in the ceiling boundary layer that affect the hydrofoil unsteady loading. This is not as clear in the 240 mm hydrofoil spectra due to contamination of the model vibrating at its (lower) natural frequency.

As α increases to 10°, the broadband peak at $f' \approx 0.2$ starts to diminish due to increased low-frequency excitations ($f' < 0.2$) attributed to self generated turbulence of the hydrofoil. Further increase in α to 20° sees the 120 mm hydrofoil stall for the smallest δ/b case and the 240 mm hydrofoil for all cases. With the 120 mm hydrofoil, the C_N spectra of the stalled case exhibits a large jump in low-frequency power that steadily decays as f' increases. This low-frequency jump at stall is attributed to the large-scale separation from the suction side of the hydrofoil with the self generated turbulence characterized by large, low-frequency disturbances. As mentioned previously, the higher δ/b cases have been able to delay stall due to the transfer of TKE.

For the 240 mm hydrofoil at 20°, all cases have completely stalled but still exhibit different spectral characteristics. The four lowest immersion cases, $\delta/b = 0.08 - 0.18$, all exhibit similar trends with a '*shoulder*' exhibiting a cut-off frequency of $f' \approx 0.15$, then levelling out between 0.2 and 0.3 before increasing again due to the hydrofoil natural frequency. On the other hand, the four highest immersion cases, $\delta/b = 0.30 - 0.45$, also possess the previously mentioned '*shoulder*' with the cut-off at $f' \approx 0.22$ before rolling off at a rate greater than that observed for the 120 mm hydrofoil.

Increasing α further to 22.5° sees the 120 mm hydrofoil stall for δ/b cases up to and including 0.28, as shown in Fig. 12. The C_N spectra of these cases (Fig. 19) show a similar low-frequency jump in power as observed at $\alpha = 20°$ for $\delta/b = 0.16$. This can also be seen in the $\delta/b = 0.35$ case where maximum C_N occurs at $\alpha = 22.5°$. Interestingly, the $\delta/b = 0.16$ case exhibits lower power than the 0.269 and 0.282 cases for $f' < 0.1$, following a similar trend to the high-immersion case of $\delta/b = 0.90$ up to $f' = 0.2$ before rolling off sharply. In the cases of $\delta/b = 0.27 - 0.35$, C_N power levels gradually roll-off as f' increases until levelling out at $f' \approx 0.15$. This is followed by the power rolling-off again past $f' = 0.2$ with power levels becoming ordered for $f' > 0.6$ with higher δ/b correlating to higher C_N power.

For the 240 mm hydrofoil at 22.5°, all δ/b cases are well beyond stall and exhibit similar C_N power levels at low frequencies ($f' < 0.01$). As f' increases, power levels gradually decrease with the roll-off being greater for lower δ/b. As f' approaches 0.2, a '*shoulder*' appears in the spectra for all cases that is more defined in the lower power cases (i.e. low δ/b). Further increase in f' sees all the C_N spectra roll-off at similar rates until reaching the peak induced by the natural frequency vibration of the hydrofoil. These characteristics, along with those observed on the 120 mm hydrofoil at 22.5°, indicate that the majority of self-generated unsteady loading from phenomena such as stall, flow separation and vortex shedding predominately occurs at relatively low frequencies, $f' < 0.2$. On the other hand, unsteady loading directly induced by the encountered ceiling boundary layer predominantly occurs at relatively high frequencies, $f' > 0.2$.

4. Conclusions

The steady and unsteady loading on a hydrofoil immersed in a turbulent boundary layer has been investigated. Measurements were obtained using model hydrofoils vertically mounted in a cavitation tunnel via static and dynamic force balances and immersed in boundary layers of varying thicknesses. The artificially thickened boundary layers were measured with the inner and outer profiles comparing well to the law of the wall and modified Coles law of the wake. For the low-immersion case with $\delta/b = 0.08$, a deviation in the normal-force curve is observed at medium to high pre-stall incidences attributed to the presence of a laminar separation bubble. The incidence in which the deviation occurs shows a *Re* dependence with the deviation being delayed with increasing *Re*. Stall in the low-immersion cases are of the sudden leading-edge type with the stall angle being delayed and width of the associated hysteresis loop increasing with *Re*. For a high-immersion case with $\delta/b = 0.81$, the normal-force slope is reduced and stall angle delayed compared to the low-immersion case attributed to increased exposure to the lower momentum flow of the ceiling boundary layer and lower aspect ratio. Additionally, it is observed with increasing immersion the reduction and eventual disappearance of the normal-force curve deviation attributed to the prevention of LSB formation from increased transfer of TKE from the ceiling to hydrofoil boundary layer. This transfer of TKE with increased immersion is also attributed to the prevention of leading-edge separation, causing a shift to trailing-edge type stall, the stall angle of which shows a strong *Re* dependence. Increasing immersion is also shown to cause the normal force standard deviation to increase linearly with δ/b.

The normal-force spectra show that for the low-immersion cases, at low incidence, the power is uniform across the measured frequency range. Increases in pre-stall incidences in low-immersion cases are shown to cause a broadband increase in excitation within an order of magnitude also across the measured frequency range. However, once stalled, there is significant amplification in the self-generated excitations, characterized by low-frequency disturbances and decreasing towards low-incidence values at $f' > 0.1$. This behaviour is associated with wake vortex shedding from leading-edge stall. In contrast, for the high-immersion case, increases in incidence have a significant effect at low frequencies, the reduced frequency range of which increases with incidence up to a $f' \approx 0.4$. Beyond $f' = 0.4$, incidence changes and hence the hydrofoil boundary layer have negligible effect. Over this region, the unsteadiness is entirely due to the wall boundary layer with a constant roll-off slope of approximately $f'^{(-3)}$. This indicates that as α increases, the frequency distribution of the self-generated excitations is increased, creating a greater population of low-frequency disturbances.

Normal-force spectra for varying δ/b at low incidence exhibit a broadband peak at $f' \approx 0.2$ that could be attributable to large-scale structures that have previously been observed in high *Re* boundary layers. The relative amplitude of this peak is seen to increase with δ/b along with the roll-off slope, converging as δ/b approaches 1. For all cases there is a general power decrease in the normal-force spectra across the measured frequency range with an increase in *Re*.

On both hydrofoils, signs of vortex-induced vibration are apparent in the normal force spectra as the first natural frequency of both hydrofoils occurs within the measured frequency range. This is exhibited on the 240 mm hydrofoil at low level of immersion where the amplitude of the resonant peak in the C_N spectra increases with incidence. In addition, the amplitude of the resonant peak is seen to increase with *Re* reflecting the more general *Re* dependence. In contrast, the 120 mm hydrofoil at a high level of immersion showed no variation in the resonant peak amplitude with incidence or *Re*. Additional features observed in the normal force spectra included local peaks in at low frequencies beyond stall on the 240 mm hydrofoil which are indicative of the coherent shedding of leading-edge structures. These results provide insight into the range of frequencies and hence size distribution in the wall boundary layer that affect the unsteady loading of the hydrofoil.

Declaration of competing interest

The authors declare that they have no known competing financial interests or personal relationships that could have appeared to influence the work reported in this paper.

Acknowledgements

This project was supported by the Research Training Centre of Naval Design and Manufacturing (RTCNDM), US Office of Naval Research (Dr. Ki-Han Kim, Programme Officer) and ONR Global (Dr. Woei-Min Lin) through NICOP S&T, Australia Grant no. N62909-11-1-7013. The RTCNDM is a University-Industry partnership established under the Australian Research Council (ARC) Industry Transformation grant scheme (ARC IC140100003). The authors would like to acknowledge the assistance of Mr Steven Kent and Mr Robert Wrigley from the Australian Maritime College for their essential help with setting up and carrying out the experiments.

References

Alamshah, S., Zander, A., Lenchine, V., 2013. Development of a technique to minimise the wind-induced noise in shielded microphones. In: Proceedings of Acoustics 2013. Australian Acoustical Society, Victor Harbour, Australia.
Alin, N., Bensow, R.E., Fureby, C., Huuva, T., Svennberg, U., 2010. Current capabilities of DES and LES for submarines at straight course. J. Ship Res. 54 (3), 184–196.
Atassi, H.M., 1984. The sears problem for a lifting airfoil revisited - new results. J. Fluid Mech. 141, 109–122.
Awasthi, M., Rowlands, J., Moreau, D., Doolan, C., 2020. The effect of aspect ratio on wall pressure fluctuations at a wing-plate junction. J. Fluids Eng..
Bailey, S., Hultmark, M., Monty, J.P., Alfredsson, P.H., Chong, M.S., Duncan, R., Fransson, J.H., Hutchins, N., Marusic, I., McKeon, B.J., et al., 2013. Obtaining accurate mean velocity measurements in high Reynolds number turbulent boundary layers using pitot tubes. J. Fluid Mech. 715, 642–670.
Baragona, M., Bijl, H., Van Tooren, M., 2003. Bubble bursting and laminar separation unsteadiness on a multi-element high lift configuration. Flow Turbul. Combust. 71 (1–4), 279–296.
Belle, A., Brandner, P.A., Pearce, B.W., de Graaf, K.L., Clarke, D.B., 2016. Artificial thickening and thinning of cavitation tunnel boundary layers. Exp. Therm Fluid Sci. 78, 75–89.
Blevins, R.D., 1979. Formulas for Natural Frequency and Mode Shape. Van Nostrand Reinhold Co., New York.
Brandner, P.A., Lecoffre, Y., Walker, G.J., 2007. Design considerations in the development of a modern cavitation tunnel. In: 16th Australasian Fluid Mechanics Conference. pp. 630–637.
Clarke, D.B., Butler, D., Crowley, B., Brandner, P.A., 2014. High-speed full-field deflection measurements on a hydrofoil using digital image correlation. In: 30th Symposium on Naval Hydrodynamics.
Del Álamo, J.C., Jiménez, J., 2009. Estimation of turbulent convection velocities and corrections to taylor's approximation. J. Fluid Mech. 640, 5–26.
Devinant, P., Laverne, T., Hureau, J., 2002. Experimental study of wind-turbine airfoil aerodynamics in high turbulence. J. Wind Eng. Ind. Aerodyn. 90 (6), 689–707.
Ducoin, A., Astolfi, J.A., Gobert, M.-L., 2012a. An experimental study of boundary-layer transition induced vibrations on a hydrofoil. J. Fluids Struct. 32, 37–51.
Ducoin, A., Astolfi, J.A., Sigrist, J.-F., 2012b. An experimental analysis of fluid structure interaction on a flexible hydrofoil in various flow regimes including cavitating flow. Eur. J. Mech. B Fluids 36, 63–74.
Glegg, S.A., Devenport, W., 2009. Unsteady loading on an airfoil of arbitrary thickness. J. Sound Vib. 319 (3–5), 1252–1270.
Goldstein, R.J., 1996. Fluid Mechanics Measurements, second ed. Taylor & Francis, Philadelphia, PA.
Goldstein, M.E., Atassi, H., 1976. A complete second-order theory for the unsteady flow about an airfoil due to a periodic gust. J. Fluid Mech. 74 (4), 741–765.
Guo, J., Julien, P.Y., Meroney, R.N., 2005. Modified log-wake law for zero-pressure-gradient turbulent boundary layers. J. Hydraul. Res. 43 (4), 421–430.
Hakkinen, R.J., Richardson Jr, A., 1957. Theoretical and Experimental Investigation of Random Gust Loads Part I: Aerodynamic Transfer Function of a Simple Wing Configuration in Incompressible Flow. Technical Report, National Advisory Commitee for Aeronautics.
Hancock, P.E., Bradshaw, P., 1983. The effect of free-stream turbulence on turbulent boundary layers. J. Fluids Eng. 105 (3), 284–289.
Hansen, K., Kelso, R., Choudhry, A., Arjomandi, M., 2014. Laminar separation bubble effect on the lift curve slope of an airfoil. In: Chowdhury, H., Alam, F. (Eds.), 19th Australasian Fluid Mechanics Conference. RMIT University.

Hoerner, S.F., Borst, H.V., 1985. Fluid-Dynamic Lift: Practical Information on Aerodynamic and Hydrodynamic Lift. Hoerner Fluid Mechanics, Brick Town, NJ.
Hoffmann, J.A., 1991. Effects of freestream turbulence on the performance characteristics of an airfoil. AIAA J. 29 (9), 1353–1354.
Hoffmann, J., Kassir, S., 1988. Effects of free-stream turbulence on turbulent boundary layers with mild adverse pressure gradients. AIAA J. 88–3757.
Howe, M., 2001. Unsteady lift and sound produced by an airfoil in a turbulent boundary layer. J. Fluids Struct. 15 (2), 207–225.
Howe, M.S., 2002. Unsteady lift produced by a streamwise vortex impinging on an airfoil. J. Fluids Struct. 16 (6), 761–772.
Huang, R.F., Lee, H.W., 1999. Effects of freestream turbulence on wing-surface flow and aerodynamic performance. J. Aircr. 36 (6), 965–972.
Hutchins, N., Marusic, I., 2007. Evidence of very long meandering features in the logarithmic region of turbulent boundary layers. J. Fluid Mech..
Jackson, R., Graham, J.M.R., Maull, D.J., 1973. The lift on a wing in a turbulent flow. Aeronaut. Q. 24 (3), 155–166.
Jones, M., Nishizawa, N., Chong, M., 2001. Experimental study of high Reynolds number turbulent boundary layers-mean flow scaling. In: 14th Australasian Fluid Mechanics Conference, Adelaide, Australia. pp. 211–214.
von Kármán, T., Sears, W., 1938. Airfoil theory for non-uniform motion. J. Aeronaut. Sci. 5 (10), 379–390.
Khoo, M., Brandner, P., Pearce, B., Clarke, D., Butler, D., Belle, A., 2015. An Australian capability for submarine control surface performance evaluation. In: MAST Asia Conference 2015. pp. 1–19.
Kirk, T.M., Yarusevych, S., 2017. Vortex shedding within laminar separation bubbles forming over an airfoil. Exp. Fluids 58 (5), 43.
Lamson, P., 1956. Measurements of Lift Fluctuations Due to Turbulence (Ph.D. thesis). California Institute of Technology.
Li, S.-W., Wang, S., Wang, J.-P., Mi, J.-C., 2011. Effect of turbulence intensity on airfoil flow: numerical simulations and experimental measurements. Appl. Math. Mech. 32, 1029–1038.
Li, M., Yang, Y., Li, M., Liao, H., 2018. Direct measurement of the sears function in turbulent flow. J. Fluid Mech. 847, 768–785.
Lissaman, P.B.S., 1983. Low-Reynolds-number airfoils. Ann. Rev. Fluid Mech. 15 (1), 223–239.
Lysak, P.D., 2011. Unsteady Lift of Thick Airfoils in Incompressible Turbulent Flow (Thesis). Pennsylvania State University.
Lysak, P.D., Capone, D.E., Jonson, M.L., 2013. Prediction of high frequency gust response with airfoil thickness effects. J. Fluids Struct. 39, 258–274.
Lysak, P.D., Capone, D.E., Jonson, M.L., 2016. Measurement of the unsteady lift of thick airfoils in incompressible turbulent flow. J. Fluids Struct. 66, 315–330.
Mack, O., 2006. A new calibration method with static loads for piezoelectric force transducers. In: XVIII IMEKO WORLD CONGRESS, Metrology for a Sustainable Development. Rio de Janeiro, Brazil.
Mayda, E., Van Dam, C., Duque, E.P., 2002. Bubble induced unsteadiness on wind turbine airfoils. In: ASME 2002 Wind Energy Symposium. American Society of Mechanical Engineers, pp. 115–125.
McKeon, B., Li, J., Jiang, W., Morrison, J., Smits, A., 2003. Pitot probe corrections in fully developed turbulent pipe flow. Meas. Sci. Technol. 14 (8), 1449.
McKeough, P.J., Graham, J.M.R., 1980. Effect of mean loading on the fluctuating loads induced on aerofoils by a turbulent stream. Aeronaut. Q. 31 (Feb), 56–69.
Mish, P.F., Devenport, W.J., 2006a. An experimental investigation of unsteady surface pressure on an airfoil in turbulence - Part 1: Effects of mean loading. J. Sound Vib. 296 (3), 417–446.
Mish, P.F., Devenport, W.J., 2006b. An experimental investigation of unsteady surface pressure on an airfoil in turbulence — Part 2: Sources and prediction of mean loading effects. J. Sound Vib. 296 (3), 447–460.
Nagib, H.M., Chauhan, K.A., Monkewitz, P.A., 2007. Approach to an asymptotic state for zero pressure gradient turbulent boundary layers. Phil. Trans. R. Soc. A 365 (1852), 755–770.
Reba, R., Kerschen, E., 1996. Influence of Airfoil Angle of Attack on Unsteady Pressure Distributions Due to High-Frequency Gust Interactions. Technical Report, NASA Langley Research Center.
Samson, A., Sarkar, S., 2016. Effects of free-stream turbulence on transition of a separated boundary layer over the leading-edge of a constant thickness airfoil. J. Fluids Eng. 138 (2), 021202.
Sears, W.R., 1941. Some aspects of non-stationary airfoil theory and its practical application. J. Aeronaut. Sci. 8 (3), 104–108.
Smits, A.J., McKeon, B.J., Marusic, I., 2011. High-Reynolds number wall turbulence. Annu. Rev. Fluid Mech. 43, 353–375.
Swalwell, K.E., Sheridan, J., Melbourne, W., et al., 2001. The effect of turbulence intensity on stall of the NACA 0021 aerofoil. In: 14th Australasian Fluid Mechanics Conference.
Theodorsen, T., 1935. General Theory of Aerodynamic Instability and the Mechanism of Flutter. Report, NACA Technical Report No. 496.
Timmer, W., 2008. Two-dimensional low-Reynolds number wind tunnel results for airfoil NACA 0018. Wind Eng. 32 (6), 525–537.
Wang, S., Zhou, Y., Alam, M.M., Yang, H., 2014. Turbulent intensity and Reynolds number effects on an airfoil at low Reynolds numbers. Phys. Fluids 26 (11), 25.
Yarusevych, S., Sullivan, P.E., Kawall, J.G., 2009. On vortex shedding from an airfoil in low-Reynolds-number flows. J. Fluid Mech. 632, 245.
Zarruk, G.A., Brandner, P.A., Pearce, B.W., Phillips, A.W., 2014. Experimental study of the steady fluid-structure interaction of flexible hydrofoils. J. Fluids Struct. 51, 326–343.